Near East Desertification: sensitivity of the local conditions leading to convection to the Dead Sea drying out

Samiro Khodayar[1,2] and Johannes Hoerner[2]

[1]Institute of Meteorology and Climate Research (IMK-TRO), Karlsruhe Institute of

 Technology (KIT), Karlsruhe, Germany

[2]Mediterranean Centre for Environmental Studies (CEAM), Valencia, Spain

Submitted to Atmospheric Chemistry and Physics

(HyMeX Inter-journal SI)

* Corresponding author. E-mail address: Khodayar_sam@gva.es (S. Khodayar)

Mediterranean Centre for Environmental Studies (CEAM),

Technological Park, Charles R. Darwin Street, 14 46980 - Paterna - Valencia - Spain

Abstract

The Dead Sea desertification-threatened region is affected by continual lake level decline and occasional, but life-endangering flash-floods. Climate change has aggravated such issues in the past decades. In this study, the impact on local conditions leading to heavy precipitation of the drying out of the Dead Sea is investigated. Sensitivity simulations with the high-resolution convection-permitting regional climate model COSMO-CLM and several numerical weather prediction (NWP) runs on an event time scale are performed over the Dead Sea area. A reference simulation covering the 2003 to 2013 period and a twin sensitivity experiment, in which the Dead Sea is dried out and set to bare soil, are compared. NWP simulations focus on heavy precipitation events exhibiting relevant differences between the reference and the sensitivity decadal realization to assess the impact on the underlying convection-related processes.

The drying out of the Dead Sea is seen to affect the atmospheric conditions leading to convection in two ways: (a) the local decrease in evaporation reduces moisture availability in the lower boundary layer locally and in the neighbouring, directly affecting atmospheric stability. Weaker updrafts characterize the drier and more stable atmosphere of the simulations where the Dead Sea has been dried out. (b) Thermally driven wind system circulations and resulting divergence/convergence fields are altered preventing in many occasions convection initiation because of the omission of convergence lines. On a decadal scale, the difference between the simulations suggests a decrease in evaporation, higher air temperatures and less precipitation.

Key Words: Dead Sea drying, climate change, convection, heavy precipitation, boundary layer, wind systems, high-resolution modelling

1. Introduction

The Eastern Mediterranean and the Middle East is a sensitive climate change area (Smiatek et al. 2011). The anticipated warming in the 21st century combined with the general drying tendency, suggest important regional impacts of climate change, which should be investigated to assess and mitigate local effects on society and ecosystems. The Dead Sea basin is dominated by semi-arid and arid climates except by the north-western part that is governed by Mediterranean climate (Greenbaum et al. 2006). It is an ideal area to study climate variation in the Near East. It was already discussed by Ashbel (1939) the influence of the Dead Sea on the climate of its neighbouring regions. The change in the climate of the Dead Sea basin caused by the drying of the Dead Sea has also been evidenced in the last decades (Alpert et al. 1997; Cohen and Stanhill 1996; Stanhill 1994). The Dead Sea is the lowest body of water in the world (~ -430 m) surrounded by the Judean Mountains (up to ~ 1 km amsl) to the west and to the east by the Maob Mountains (up to ~ 3 km amsl). The area in between is rocky desert. The complex topography of the area favours the combined occurrence of several wind regimes in addition to the general synoptic systems, namely valley and slope winds, Mediterranean breezes and local lake breezes (e.g. Shafir and Alpert 2011). These wind systems are of great importance for the living conditions in the region since they influence the visibility and the air quality (e.g. Kalthoff et al. 2000; Corsmeier et al. 2005) as well as the atmospheric temperature and humidity. Since the Dead Sea is a terminal lake of the Dead Sea Valley, no natural outflow exists; evaporation is the main loss of water. The wind velocity and vapour pressure deficit are identified as the main governing factors of evaporation throughout the year (Metzger et al. 2017). Through the high evaporation the lake level declines and results in a desertification of the shoreline and a changing fraction of water and land surface in the valley. The documented Dead Sea water level drop of about 1 m/y in the last decades (Gavrieli et al. 2005) is mainly due to the massive water consumption at its upstream having climate changes a small contribution to the lake level decrease (Lensky and Dente 2015). This situationseverely affects agriculture, industry and the environmental conditions in the area, thus, leading to substantial economic losses (Arkin and Gilat 2000).

The Jordan River catchment and Dead Sea exhibit in the north, annual precipitation in the order of 600-800 mm, whereas in the south, there is an all year arid climate with an annual precipitation of <150 mm (Schaedler and Sasse 2006). Rain occurs between October and May and can be localized or widespread (Dayan and Sharon 1980) (Sharon and Kutiel 1986). Rainfall varies seasonally and annually, and it is often

concentrated in intense showers (Greenbaum et al. 2006) caused mainly by severe convection (Dayan and Morin 2006). Flash floods are among the most dangerous meteorological hazards affecting the Mediterranean countries (Llasat et al 2010), thus, knowledge about the processes shaping these events is of high value. This is particularly relevant in arid climates, where rainfall is scarce, and often, local and highly variable. In flood-producing rainstorms, atmospheric processes often act in concert at several scales. Synoptic-scale processes transport and redistribute the excess sensible and latent heat accumulated over the region and subsynoptic scale processes determine initiation of severe convection and the resulting spatio-temporal rainfall characteristics. The main responsible synoptic weather patterns leading to heavy rainfall in the region are in general well known and described in previous publications (e.g. Belachsen et al. 2017; Dayan and Morin 2006). Belachsen et al. (2017) pointed out that three main synoptic patterns are associated to these heavy rain events: Cyprus low accounting for 30% of the events, Low to the east of the study region for 44%, and Active Read Sea Trough for 26%. The first two originate from the Mediterranean Sea, while the third is an extension of the Africa monsoon. Houze (2012) showed that orographic effects lead to enhanced rainfall generation; rain cells are larger where topography is higher. Sub-synoptic scale processes play a decisive role in deep convection generation in the region. Convection generated by static instability seems to play a more important role than synoptic-scale vertical motions (Dayan and Morin 2006). The moisture for developing intensive convection over the Dead Sea region can be originated from the adjacent Mediterranean Sea (Alpert und Shay-EL 1994) and from distant upwind sources (Dayan and Morin 2006).

In this study, the sensitivity of the local conditions in the Dead Sea region to the drying out of the Sea is investigated focusing on the conditions leading to heavy precipitating convection in the region. The relevance of the Dead Sea as a local source of moisture for precipitating convection as well as the impact of the energy balance partitioning changes and related processes caused by the drying of the Dead Sea are investigated. With this purpose, a sensitivity experiment with the high-resolution regional climate model COSMO-CLM [Consortium for Small scale Modelling model (COSMO)-in Climate Mode (CLM); Böhm et al. 2006] is conducted. The high horizontal grid spacing used (~ 2.8 km) resolves relevant orographic and small-scale features of the Dead Sea basin, which is not the case when coarser resolution simulations are performed. Moreover, at this resolution convection is explicitly resolved instead of being parametrized, which has been already extensively demonstrated to be highly beneficial for the simulation of heavy precipitation and convection-related processes. The benefit

104 of employing high-resolution convection permitting simulations is mainly in sub-daily
105 time-scales, (e.g., Prein et al., 2013; Fosser et al., 2014; Ban et al., 2014), however,
106 daily precipitation is also positively affected, particularly in winter time (Fosser et al.,
107 2014). Previous studies in the area applying high-resolution modelling agree with the
108 beneficial impact of finer resolution against coarser ones (e.g. *Rostkier-Edelstein et al.*
109 *2014; Hochman et al. 2018; Kunin et al. 2019*).

110 A decadal simulation and several event-based Numerical Weather Prediction (NWP)
111 runs covering the eastern Mediterranean are carried out. A process understanding
112 methodology is applied to improve our knowledge about how sub-synoptic scale
113 processes leading to severe convection are affected by the drying of the Dead Sea.
114 The article is organized as follows. Section 2 provides an overview of the data and the
115 methodology used. Then, in section 3, the climatology of the region based on the high-
116 resolution convection-permitting decadal simulation is presented and the impact of
117 drying out the Dead Sea is examined across scales. Finally, conclusions are discussed
118 in section 4.

119

2. Data and methodology

2.1 The COSMO-CLM model

122 In this investigation, the regional climate model (RCM) of the non-hydrostatic COSMO
123 model, COSMO-CLM (CCLM), is used (Version 5.0.1). It has been developed by the
124 Consortium for Small-scale modeling (COSMO) and the Climate Limited-area Modeling
125 Community (CLM) (Böhm et al., 2006). It uses a rotated geographical grid and a
126 terrain-following vertical coordinate. The model domain covers the southern half of the
127 Levant, centred around the Dead Sea, with a horizontal resolution of 7 km and 2.8 km,
128 60 vertical levels and a time step of 60 and 20 seconds, respectively. Using IFS
129 (Integrated Forecasting System) analysis, the spectral weather model of ECMWF
130 (European Centre for Medium-Range Weather Forecast) as driving data for the
131 simulations, a double nesting procedure was employed. The coarsest nest at 0.0625º
132 resolution (about 7 km) covers 250 grid points in x direction and 250 grid points in y
133 direction. The size and location of the 7 km domain has been considered large enough
134 to take into consideration all possible synoptic situations relevant for the development
135 of extreme phenomena in the study area as well as the influence of the Mediterranean
136 Sea. The finest nest at 0.025º (circa 2.8 km) covers 150 x 150 grid points, thus a total

137   area of 22500 grid points and includes the study area (72 grid point in x direction and
138   92 in y direction) centred around the Dead Sea.

139   A Tiedtke (1989) mass-flux scheme is used for moist convection in the 7 km, and
140   reduced Tiedke mass-flux scheme for shallow convection. Contrary to the CCLM-7 km
141   simulation, where convection is parameterized, in the CCLM-2.8 km convection is
142   explicitly resolved (Doms and Baldauf, 2015), so only the reduced Tiedke mass-flux
143   scheme is used for shallow convection. The model physics includes a cloud physics
144   parameterization with 5 types of hydrometeors (water vapor, cloud water, precipitation
145   water, cloud ice, precipitation ice), a radiative transfer scheme based on a delta-two-
146   stream solution (Ritter and Geleyn, 1992) and a roughness-length dependent surface
147   flux formulation based on modified Businger relations (Businger et al., 1971).

148   Orography data from GLOBE (Global Land One-km Base Elevation Project) of NOAA
149   (National Oceanic and Atmospheric Administration) and soil data from HWSD
150   (Harmonized Worlds Soil Database) TERRA is used. HWSD is a global harmonization
151   of multiple regional soil data sets with a spatial resolution of 0.008° (FAO, 2009),
152   resulting in 9 different soil types in the model, namely 'ice and glacier', 'rock / lithosols',
153   'sand', 'sandy loam', 'loam', 'loamy clay', 'clay', 'histosols', and 'water'.

154   Multiple model runs have been performed. A 7 km run from 2003 to 2013 with daily
155   output is used as nesting for two 2.8 km runs over the same time span. The Dead Sea
156   is dried out and replaced with soil types from the surrounding area in one of them
157   (SEN), the other one is used as reference (CLIM). For the detailed investigation of
158   convective events on 14.11.2011 and 19.11.2011, sub-seasonal simulations have been
159   performed with the same settings as the decadal simulation, but with additional hourly
160   output.

161   **2.2 Methodology**

162   A decadal simulation covering the 2003 to 2013 time period was carried out with the
163   convection permitting 2.8 km COSMO-CLM model. Lateral boundary conditions and
164   initial conditions are derived from the European Centre for Medium-Range Weather
165   Forecasts (ECMWF) data. The COSMO-CLM 7 km is used as nesting step in between
166   the forcing data and the 2.8 km run. This reference simulation will be hereafter referred
167   to as REF^{CLIM} simulation. Parallel to this, a sensitivity experiment (hereafter SEN^{CLIM}) is
168   carried out in which the Dead Sea is dried out and set to bare soil on -405 m level
169   (depth of the Dead Sea in the external data set, GLOBE (Hastings and Dunbar, 1999)).

170 After examination of the results, the first year of simulations is considered spin-up time,
171 thus, our analysis covers the 2004-2013 period.

172 The precipitation field has been validated using the EOBS dataset (resolution of 0.1°
173 and available for the period 1980-2011; Haylock et al. 2008), and the APHRODITE's
174 (Asian Precipitation - Highly-Resolved Observational Data Integration Towards
175 Evaluation: Yatagai et al. 2008, 2012) daily gridded precipitation, resolution of 0.25º
176 and available for 1980-2007. The APHRODITE data shows generalized lower
177 precipitation values than EOBS, but still higher than our simulation particularly close to
178 the northern Mediterranean shoreline, over coastal-flat terrain, whereas the best
179 agreement is at areas dominated by complex terrain. Despite these biases the
180 comparison of the temporal areal-mean of the model simulations at 7 km and 2.8 km
181 and the APHRODITE dataset demonstrates that in general the model quite well
182 captures the precipitation events. An improvement is seen at the finer resolution.

183 Regional dry and wet periods are identified and quantified in the simulations by means
184 of the Effective Drought Index (EDI; Byun and Wilhite 1999; Byun and Kim 2010). The
185 EDI is an intensive measure that considers daily water accumulations with a weighting
186 function for time passage normalizing accumulated precipitation. The values are
187 accumulated at different time scales and converted to standard deviations with respect
188 to the average values. Here we use an accumulation period of 365 days. EDI dry and
189 wet periods are categorized as follows: moderate dry periods -1.5 <EDI<-1, severe dry
190 periods -2<EDI<-1.5, and extreme dry periods EDI<-2. Normal periods are revealed by
191 -1<EDI<1 values.

192 Based on daily mean values, precipitation and evapotranspiration distribution and
193 possible tendencies in the 10-year period are assessed. To further asses the most
194 affected areas in our study area, this is divided in four subdomains surrounding the
195 Dead Sea and trying to respect the orographic pattern in the area (Figure 3). Annual
196 cycles are thus separately investigated to take into consideration the relevant
197 differences in orography, soil types, and distance to the coast among others (Figure1),
198 which are known to have a significant impact in the precipitation distribution in the
199 region (e.g. Belachsen 2017; Houze 2012). . Differences in the annual cycle and
200 temporal evolution of precipitation and evapotranspiration between the REF^{CLIM} and
201 SEN^{CLIM} are discussed. Also, differences in the near-surface and boundary layer
202 conditions and geopotential height patterns are examined. Geographical patterns of
203 mean evapotranspiration and precipitation and differences with respect to the reference
204 simulation are assessed. Probability distribution functions (PDFs), and the Structure,

205 Amplitude and Location (SAL: Wernli et al. 2008) analysis methodologies are used to
206 illustrate differences in the mean and extreme precipitation between the reference and
207 the sensitivity experiments. The SAL is an object-based rainfall verification method.
208 This index provides a quality measure for the verification of quantitative precipitation
209 forecasts considering three relevant aspects of precipitation pattern: the structure (S),
210 the amplitude (A), and the location (L). The A component measures the relative
211 deviation of the domain-averaged rainfall; positive values indicate an overestimation of
212 total precipitation, negative values an underestimation. The component L measures the
213 distance of the center of mass of precipitation from the modelled one, and the average
214 distance of each object from the center of mass. The component S is constructed in
215 such a way that positive values occur if precipitation objects are too large and/or too
216 flat and negative values if the objects are too small and/or too peaked, quantifying the
217 physical distance between the centres of mass of the two rainfall fields to be compared.
218 Perfect agreement between prediction and reference are characterized by zero values
219 for all components of SAL. Values for the amplitude and structure are in the range (−2,
220 2), where ±0.66 represents a factor of 2 error. The location component ranges from 0
221 to 2, where larger values indicate a greater separation between centres of mass of the
222 two rainfall fields. This is done by selecting a threshold value of 1/15 of the maximum
223 rainfall accumulation in the domain (following Wernli et al. 2008). The structure and
224 location components are thus independent of the total rainfall in the domain.

225

226 Differences in the temporal evolution of precipitation between the REF^{CLIM} and SEN^{CLIM}
227 are identified. In Table 1, those events in which an area-mean (study area, Figure 1)
228 difference between both simulations higher than ±0.1 mm/d exists are selected as
229 potential heavy precipitation events and classified attending to their synoptic scale
230 environment and atmospheric stability conditions (Table 1).

231 Although Dayan and Morin (2006) discuss that in general large-scale vertical motions
232 do not provide the sufficient lifting necessary to initiate convection, it was demonstrated
233 by Dayan and Sharon (1980) that a relationship exists between the synoptic-scale
234 weather systems and deep moist convection, being those systems responsible for the
235 moisturizing and destabilization of the atmosphere prior to convective initiation. They
236 pointed out that indices of instability proved the most efficient determinants of the
237 environment characterizing each rainfall type in the region. Thus, two indicators of the
238 atmospheric degree of stability/instability, namely the Convective Available Potential
239 Energy (CAPE; Moncrieff and Miller 1976) and the KO-index (Andersson et al. 1989),
240 are examined in this study. The CAPE is a widely known index indicating the degree of

241 conditional instability. Whereas, the KO-index, which is estimated based on the
242 equivalent potential temperature at 500, 700, 850 and 1000 hPa (following the
243 recommendations by Bolton 1980), describes the potential of deep convection to occur
244 as a consequence of large-scale forcing (Andersson et al. 1989; Khodayar et al. 2013).
245 Generally, regions with KO-index < 2 K and large-scale lifting are identified as
246 favourable for deep convection. Parcel theory (50 hPa ML (Mixed Layer) parcel) and
247 virtual temperature correction (Doswell and Rasmussen 1994) are applied to these
248 calculations.

249 Based on the above criteria, a separation was made between events with widespread
250 rainfall and those more localized. Among the latter, we selected two events to illustrate
251 the local impacts on the boundary layer conducive to deep moist convection.
252 Particularly, differences in the amount, structure and location of precipitation are
253 assessed by examining the spatial patterns and the SAL verification method. The two
254 selected events for detail analysis in this study are those showing the larger SAL
255 deviations. Those two cases occur close in time, but they are not the same event. No
256 differences in the soil and atmospheric conditions have been found in the period
257 between the events when the REF and SEN simulations are compared.   Even though
258 a more detail analysis is provided for the two selected cases, all convective-events
259 listed in Table 1 have been examined to assess the main impacts on the mechanisms
260 leading to convection. High-resolution simulations with the NWP COSMO 2.8 km model
261 are performed with hourly output temporal resolution and covering a 3-day period
262 (including 48-h prior to the day of the event, from 00 UTC) to capture atmospheric pre-
263 conditions conducive to deep moist convection.   For this, a reference simulation,
264 REF^{NWP}, and a sensitivity experiment, SEN^{NWP}, are carried out for each event.

265 We have to point out that the external data sets commonly employed describing
266 relevant features of the Dead Sea region, such as the depth, shape and orography of
267 the Dead Sea, as well as Dead Sea water characteristics at the reference run, do not
268 accurately represent the reality. In the same direction, biases in relation to different
269 variables such as the precipitation field and evaporation over the Dead Sea have to be
270 considered.

271

272 **3. Results and discussion**

273 **3.1 Climatology of the Dead Sea region**

274 *Annual cycle*

275   To assess the climatology of the study region (Figure 1) the annual evaporation and
276   precipitation cycles based on daily means of the respective quantities are investigated
277   (Figure 2). Additionally, we examine the evolution of specific humidity (Qv_{2m}) and
278   temperature at 2 m (T_{2m}) as well as total column integrated water vapour (IWV) and
279   low-boundary layer (< 900 hPa) equivalent potential temperature (Θ_e). Possible
280   changes in the atmospheric stability conditions are evaluated by examination of the
281   CAPE and KO-index. In Figure 2, all grid points over the study region (Figure 1) and
282   the time period 2004-2013 are considered. Differences between the REF^{CLIM} and the
283   SEN^{CLIM} simulations are also discussed.

284   The annual cycle of evaporation shows minimum values in the autumn season (around
285   October, ~ 0.1 mm/d) and maximum evaporation in spring (around March, ~ 0.4 mm/d).
286   The dependency with the precipitation cycle is clear with maximum values of the latter
287   around March and rain occurring between October and May (Figure 2a) in agreement
288   with observations in the area (Dayan and Sharon 1980). The difference between the
289   evaporation in the REF^{CLIM} and the SEN^{CLIM} simulations indicates a mean decrease in
290   the order of 0.02 (February) to ~ 0.1 (August) mm/d in the absence of the Dead Sea
291   water (SEN^{CLIM}). The largest difference is in the dry period (May to October) when
292   water availability is less dependent on precipitation, and evaporation is higher over the
293   Dead Sea in contrast to the minimum values over land (Metzger et al. 2017). In
294   general, there is a decrease of about 0.5 % in mean precipitation in the SEN^{CLIM}
295   simulation. In contrast to the differences in evaporation, precipitation differences
296   between the reference and the sensitivity experiment occur in both directions during
297   the rain period, from October to May. Examining the total number over the whole
298   decadal simulation it is seen that the number of dry or wet days (> 0.1 mm/d) or heavy
299   precipitation events is not largely affected in the sensitivity experiment. In general, the
300   number of dry days increases (fewer wet days) in the SEN^{CLIM} simulation, whereas the
301   number of high intensity events show almost no variation. For each simulation, the
302   difference between precipitation and evaporation is negative mainly in spring and
303   summer contributing to the dryness in the region. Furthermore, the difference between
304   the REF^{CLIM} and SEN^{CLIM} simulations indicates that PREC-EVAP is higher in the
305   SEN^{CLIM} simulation probably in relation to the reduced evaporation over the dry sea
306   area and the general decrease in the precipitation amount in the region.

307   In addition to the reduced evaporation and precipitation (about 0.5 %) in the whole
308   domain in the SEN^{CLIM} simulation a drier and warmer lower-troposphere is identified
309   (Figure 2b) in agreement with the observational assessment by Metzger et al. (2017) of
310   the cooling effect of evaporation on air temperature in the region. The annual cycle of

311 IWV and $\Theta_{e<900hPa}$ in Figure 2c show that the impact of the dry Dead Sea resulting

312 evaporation is less pronounced when a deeper atmospheric layer is considered.

313 Indeed, $\Theta_{e<900hPa}$ evolution evidences that the warming effect due to the decreased

314 evaporation in the SEN^{CLIM} simulation is restricted to the near surface.

315 In Figure 2d, the annual cycle of areal mean CAPE displays larger values in the period

316 from August to November, being this the period more favourable for convection.

317 Negative CAPE differences between the REF^{CLIM} and the SEN^{CLIM} simulations are

318 presumably in relation to the identified distinct lower-atmospheric conditions, being

319 these more favourable and consequently CAPE values higher in the REF^{CLIM}

320 simulation. In the same period, the KO-index indicates a more potentially unstable

321 atmosphere, i.e. prone to deep convection because of large-scale forcing, and larger

322 differences between simulations.

323 In agreement with the well-known precipitation distribution in the region most of the

324 events occur in A1 (north-west) and A2 (north-east). Also, in these subdomains larger

325 differences between the REF^{CLIM} and SEN^{CLIM} simulations are identified pointing out the

326 relevance of the Dead Sea evaporation in the pre-convective environment for rainfall

327 episodes over the study area (Figure3a). Considering only land grid points almost no

328 difference between simulations is found in the evaporation annual cycle of A1 and A2

329 (Figure3b) suggesting the distinct amount of moisture advected towards A1 and A2

330 from the Dead Sea in REF^{CLIM} and SEN^{CLIM} as responsible for the differences in the

331 boundary layer conditions conducive to convection. Also, in these subdomains the

332 dryer and warmer lower boundary layer and the reduced instability in the SEN^{CLIM} are

333 recognized

334 *Inter-annual variability*

335 In Figures 4 we discuss the inter-annual variability (based on monthly-daily areal mean

336 values) of evaporation, precipitation as well as drought evolution.

337 The reduced evaporation in the annual cycle of the SEN^{CLIM} simulation for the whole

338 investigation domain, resulting from the drying of the Dead Sea and affected

339 evaporation, remains from year to year (Figure 4a). Larger differences between the

340 simulations occur in the May to November months in agreement with the annual cycle

341 in Figure 2a. This, and the time period of the maximum/minimum is constant over the

342 years. A tendency towards lower evaporation at each simulation and higher differences

343 between both at the end of the period are identified. An inter-annual fluctuation is

344 observed in both REF^{CLIM} and SEN^{CLIM} simulations. The yearly rate of evaporation

345   shows, for example, in REF^{CLIM} maximum values of about 7 mm in 2011 and around 17
346   mm in 2012. This is in agreement with the positive correlation expected between
347   precipitation and evaporation, a trend towards decreased precipitation and a
348   correspondence between drier years such as the 2011-2012 period and lower annual
349   evaporation are seen in Figure 4b. Year to year EDI calculations in Figure 4c help us
350   identify the regional extreme dry and wet periods. The EDI range of variation from
351   about -1 to 2 for the whole period of simulation indicates that the dry condition is the
352   common environment in the area, while the wet periods, EDI up to 6, could be
353   identified as extreme wet periods (relative to the area), in this case in the form of heavy
354   precipitation events. Maximum positive EDI values are in the first months of the year in
355   agreement with the precipitation annual cycle in Figure 2, whereas minimal EDI values
356   occur in summer and autumn indicative of the dry conditions in these periods.
357   Differences in the EDI calculations from both simulations reveal distinct precipitation
358   evolutions and denote timing differences in the occurrence of the precipitation events.
359   When the regional climate evolution is examined in combination with the impact on the
360   number of heavy precipitation events (Table 1) the impact is stronger in the dry period
361   of 2011 (Figure 4a). About six events show relevant differences in this period, contrary
362   to the average 3 episodes per year.

363   *Spatial distribution*

364   The geographical patterns of evaporation and precipitation are presented in Figure 5.
365   Over the Dead Sea, the simulated average annual evaporation for the period under
366   consideration is in the order of 1500-1800 mm/y, in contrast to the values in the deserts
367   east and south, where the evaporation is less than 20 mm/y. Observed annual
368   evaporation of this lake is known to be about 1500 mm and to vary with the salinity at
369   the surface of the lake and freshening by the water inflow (Dayan and Morin 2006;
370   Hamdani et al. 2018). Over land, higher evaporation is seen over the Judean
371   Mountains and the Jordanian Highlands. High correlation with the orography and soil
372   types is seen (Figure 1). Evaporation is probably correlated with rainfall which in turn is
373   correlated with topography. Particularly, in the Jordanian Highlands where maximum
374   evaporation is around 200 mm/y, the complex topography coincides with sandy loam
375   soils, whereas most of the soil in study region is defined as loamy clay or clay (Figure
376   1). The evaporative difference field between simulations in Figure 5a shows a highly
377   inhomogeneous patchiness not evidencing any relationship with orography or soil type,
378   but rather with changes in the precipitation pattern in the SEN^{CLIM} simulation as seen in
379   Figure 5b.

380   In agreement with the temporal series of areal mean precipitation in Figure 3 higher

381   annual precipitation are in the north-west and -east, with respect to the southern

382   regions. Topographic features exert a large impact on precipitation distribution with

383   maxima of about 175 to 300 mm/y over the Judean Mountains and the Jordanian

384   Highlands. To the northern end of the Dead Sea valley, the largest precipitation

385   difference between the REF^{CLIM} and the SEN^{CLIM} simulations is identified, rather than

386   directly over the Dead Sea area noting the importance of advected moisture from the

387   Dead Sea evaporative flux upslope and along the Dead Sea valley as well as the

388   indirect effects of a different spatial distribution of low-tropospheric water vapour in the

389   occurrence of precipitating convection.

390   Regarding the impact on the large-scale conditions, differences in the spatial pattern

391   and strength of the 500 hPa geopotential height field are identified over the Dead Sea

392   (not shown). In the 10-year mean, differences up to 0.002gpdm higher in SEN than in

393   REF are observed. Around the Dead Sea area, the differences are smaller and more

394   irregular. Generally, the differences are higher in the east of the Dead Sea than in the

395   west.

396   *Precipitation probability distribution function*

397   While the probability for lower intensity precipitation is very similar in the REF^{CLIM} and

398   the SEN^{CLIM} simulations differences are recognized in the higher precipitation

399   intensities, from about 150 mm/d (Figure 6a). Particularly, above 180 mm/d extreme

400   precipitation values occur less frequent at the SEN^{CLIM} simulation where a drier,

401   warmer and more stable atmosphere is identified (Figure 2).

402   *SAL*

403   The use of the SAL method in this study differs from the approach frequently presented

404   in literature since it is here not our purpose to examine differences between the

405   simulated field and observations (adequate observations for this comparison are not

406   available in the area), but to compare changes regarding the structure, amount and

407   location of the precipitation field between our reference and sensitivity experiments.

408   Figure 6b shows that when the mean precipitation over the whole simulation period is

409   considered all three SAL components are close to zero, meaning that very small

410   differences are found. However, when single precipitation events in the REF^{CLIM}

411   simulation are compared with the same period at the SEN^{CLIM} simulation, larger

412   differences regarding structure, amount and location of rainfall events are found. For

413   further examination of this issue two exemplary heavy precipitation events (indicated by

414   boxes in Figure 6b) are analysed in detail. In both cases, a negative A-component is

415   recognized, that is, less precipitation falls in the SEN[CLIM] simulation. The S-component

416   also evidences the change in the structure of the convective cells. The L-component is

417   low meaning that the convective location does not change significantly in the SEN[CLIM]

418   simulation, in contrast to the intensity and structure of the cells.

419

420   **3.2 Sensitivity of atmospheric conditions to the Dead Sea drying: episodic**

421   **investigation**

422   Among those events exhibiting differences in the precipitation field between both

423   simulations (Table 1 and Figure 6b) two situations occurring in the time period of the 14

424   to 19 November 2011 are investigated in the following.

425   In this term, the synoptic situation is characterized by a Cyprus low and its frontal

426   system located over the Dead Sea at about 00 UTC on the 15 November 2011 and at

427   12 UTC on the 18 November 2011. The low-pressure system and its frontal system

428   induced strong south-westerly to westerly winds with mean wind velocities up to 15

429   m/s.

430   In the first situation (hereafter CASE1), in association with the western movement of

431   the cold front a convective system develops over the Jordanian Highlands with

432   precipitation starting at about 21 UTC on the 14 November 2011. This convective

433   system is of high interest because of the large difference in its development between

434   the REF[14.11] and the SEN[14.11] simulations.

435   In Figure 7a the 24-h accumulated precipitation, from 14.11 09 UTC to 15.11 08 UTC,

436   in the investigation area is shown for the REF[14.11] and the SEN[14.11] simulations. Two

437   precipitation areas are seen, on the north-western and north-eastern of the Dead Sea.

438   Larger difference between models is on the north-eastern region (24-h accumulated

439   precipitation > 100 mm/d in REF[14.11], while < 50 mm/d in SEN[14.11]), which is the focus of

440   our analysis.

441

442   The REF[14.11] simulation shows that in the 6 hours period prior to the initiation of

443   convection the pre-convective atmosphere and more specifically the lower boundary

444   layer exhibit a moist (IWV ~ 24-30 mm, qvPBLmax ~ 7-10 g/kg) and unstable (CAPE ~

445   1100 J/kg; KO-index ~ -8 K; not shown) air mass on the western side of the

446   investigation area, particularly close to the western Mediterranean coast, and drier

447   (IWV~ 8-16; qvPBLmax ~ 4-6 g/kg) and more stable conditions (CAPE< 200 J/kg; KO-

448 index ~ 0-2 K) on the eastern side of the domain (Figure 7b). A maximum difference of
449 about 5 g/kg from west to east is established in the lower boundary layer.

450 Main differences between both simulations are over the Dead Sea (IWV difference up
451 to 2 mm and qvPBL up to 1.5 g/kg) and north and north-east of it, but almost similar
452 conditions everywhere else. In our target area (subdomain of investigation where the
453 convection episode takes place (red box in Figure 7)), north-east of the Dead Sea, a
454 drier and a more stable atmosphere is identified at the SEN[14.11] simulation.

455 The evolution of the wind circulation systems in the area is similar in both simulations
456 (Figure 7c). The 700 hPa, 850 and 950 hPa winds dominantly blow from the south
457 south-west during the pre-convective environment advecting the moist unstable air
458 mass towards the Dead Sea valley and north-east of it, directly affecting the
459 atmospheric conditions at the target area (for a comparison with a climatology of the
460 wind conditions in the region please see Metzger et al. 2017). In both simulations, the
461 passage of the cold front over the Dead Sea establishes a strong southerly wind from
462 about 10 UTC on the 14 November 2011.

463 Prior to this time, dry air was advected below about 850 hPa towards the target area
464 from the east. The turning of the low-level winds and the resulting moistening of the
465 atmosphere is well and equally captured by both simulations (Figure 8a). Furthermore,
466 at the near-surface, from about 16 UTC, ~ 5 h prior to convection initiation in the target
467 area, a near-surface convergence line forms at the foothills of the northern part of the
468 Jordanian Highlands, which is also well and equally captured by both simulations
469 (Figure 8b). The lifting provided by the convergence line triggers convection in the
470 area. However, the drier and more stable atmosphere in the SEN[14.11] simulation results
471 in less intense convection, weaker updrafts, and reduced precipitation at the eastern
472 slope of the valley.

473

474 In the second case, CASE2, we address an episode of localized convection taking
475 place on the north-western edge of the Dead Sea in the REF simulation, whereas no
476 convection develops in the SEN simulation. The isolated convection in the REF
477 simulation left about 50 mm rain in 3 h starting at about 03 UTC on the 19 November
478 2011 (Figure 9).

479 In contrast to CASE1, the modification of the pre-convective environment relevant for
480 convective initiation is in this case dominated by dynamical changes in the mesoscale
481 circulations. Differences in the evolution and strength of the Mediterranean Sea Breeze
482 (MSB), the Dead Sea breeze and orographic winds influence atmospheric conditions in
483 the target area leading to the assistance to or to the absence of convection. The most

484   significant difference observed between the simulations is in the development of a
485   strong near-surface convergence line in the REF simulation (which is not present in the
486   SEN simulation hindering convection in the area), which forms about 2 h before
487   convective initiation (Figure 10).

488   Even in the first hours of the 18 November 2011 differences in the speed and direction
489   of the near-surface winds over the Dead Sea and on the eastern flank of the Jordanian
490   Highlands could be identified. A fundamental difference between simulations occurs
491   from about 17 UTC when strong westerly winds indicating the arrival of the MSB reach
492   the western shore of the Dead Sea. One hour later, in the REF[19.11] run the MSB
493   strongly penetrates the Dead Sea valley reaching as far as the eastern coast in the
494   centre to south areas. However, in the SEN[19.11] simulation the MSB does not penetrate
495   downward, instead strong northerly winds flow along the valley (Figure 10a). Numerous
496   observational and numerical studies carried out to investigate the dynamics of the MSB
497   (e.g. Naor et al. 2017; Vuellers et al. 2018) showed that the downward penetration of
498   the MSB results from temperature differences between the valley air mass, which is
499   warmer than the maritime air mass. An examination of temperature differences along a
500   near-surface north-south valley transect (positions in Figure 10a) indicates a decrease
501   of about 4 °C at the near-surface over the dried Dead Sea area in contrast to negligible
502   changes on a parallel transect inland, on the western coast of the Dead Sea. These
503   evidences the notorious impact of the absence of water in the valley temperature, thus,
504   gradients in the region. The colder valley temperatures do not favour the downward
505   penetration of the MSB, which strongly affects the atmospheric conditions in the valley.
506   Moreover, a north-easterly land breeze is visible from about 20 UTC on the eastern
507   shore of the Dead Sea in the REF[19.11] simulation, but not in the SEN[19.11] simulation
508   (Figure 10b). This situation reflects an interesting case different from the ones
509   generally presented in former investigations in the area (e.g. Alpert et al. 1997 ; and
510   Alpert et al. 2006b) in which due to the recent weakening of the Dead-Sea breeze,
511   mainly because of the drying and shrinking of the Sea, the Mediterranean breeze
512   penetrates stronger and earlier into the Dead-Sea Valley increasing the evaporation
513   because of the strong, hot and dry wind.

514   Mountain downslope winds develop in both simulations from about 22 UTC. One hour
515   later, strong northerly valley flow in the northern part of the Dead Sea contrasts with the
516   westerly flow in the SEN[19.11] simulation (Figure 10c). As the valley cools down during
517   night time in the SEN simulation, T2m decreases about 1 K from 20 UTC to 03 UTC in
518   contrast with the 0.1 K decrease of the Dead Sea in the REF simulation, the
519   temperature gradient weakens and the northerly valley flow present in the REF

520   simulation is absent in the SEN simulation. During the night, the synoptic conditions
521   gain more influence than the local wind systems governing the conditions in the valley
522   during day time. South-easterly winds prevail in the valley in both simulations. Much
523   stronger wind velocities are reached in the REF simulation, confirming the sensitivity of
524   large-scale dynamics to near-surface climate change-induced impacts.

525   The encounter of the north north-westerly and south south-easterly winds over the
526   Dead Sea area in the REF[19.11] simulation induces the formation of a convergence zone,
527   which intensifies and extends offshore over the next hours and determines the location
528   of convective initiation. Meanwhile, homogeneous south-easterly winds are observed in
529   the SEN simulation (Figure 10d).

530   The differences in the wind circulations contribute to a different distribution of the
531   atmospheric conditions in the target area, particularly, low-tropospheric water vapour
532   as seen in the vertical cross sections in Figure 11. The evolution of the atmospheric
533   conditions in the 3-h period prior to convective initiation evidences the deeper and
534   wetter boundary layer in the REF[19.11] simulation at the north-western foothills of the
535   ridge at the Jordanian Highlands. Differences of IWV up to 2 mm, and of instability
536   (CAPE) close to 200 J/kg are found in this area (not shown). This is the location of the
537   convergence line where convective updrafts, which start close to the ground, are
538   triggered reaching a maximum vertical velocity of about 5 m/s above the convergence
539   zone in the REF[19.11] simulation.

540

4. Conclusions

542   The drying and shrinking of the Dead Sea has been extensively investigated in the last
543   decades from different points of view. This process has been related to significant local
544   climate changes which affect the Dead Sea valley and neighboring regions. The
545   climate of the Dead Sea is very hot and dry. But occasionally the Dead Sea basin is
546   affected by severe convection generating heavy precipitation, which could lead to
547   devastating flash floods.

548   In this study, high-resolution COSMO model simulations are used to assess the
549   sensitivity of Dead Sea changes on the occurrence of convective precipitation in the
550   region. A set of high-resolution, ~ 2.8 km, climate simulations covering the period 2003
551   to 2013, and several numerical weather prediction (NWP) runs on an event time scale
552   (~ 48-36 h) are performed over the Dead Sea area. On a decadal time scale, two
553   simulations are carried out. The first "reference" run with the Dead Sea area, and a

second run "sensitivity" in which the Dead Sea is dried out and set to bare soil. The NWP simulations focus on two heavy precipitation events exhibiting relevant differences between the reference and the sensitivity decadal runs. A total of four simulations are performed in this case.

As the energy balance partitioning of the Earth's surface changes due to the drying of the Dead Sea, relevant impacts could be identified in the region. From a climatological point of view, the drying out of the Dead Sea results in less evaporation, higher air temperatures and less precipitation. Reduced evaporation over the Dead Sea occurs from May to October. The cooling effect of evaporation in the neighboring areas results in an increase of T-2m. Atmospheric conditions, such as air temperature and humidity, are mostly affected in the lower-tropospheric levels, which in turn influence atmospheric stability conditions, hence, precipitating convection. In general, the number of dry/wet days is not largely affected by the drying out of the Dead Sea, although these differences could be larger for hourly precipitation; rather the structure and intensity of the heavier precipitation events is changed. While a general and homogeneous decrease in evaporation is seen at the SEN^{CLIM} simulation, precipitation deviations occur in both directions, which could suggest and impact on the timing of the events. A relevant year to year variability is observed in evaporation-precipitation which indicates the need of long time series of observations to understand local conditions and to validate model simulations.

The detailed analysis of two heavy precipitation events allowed us to further assess the possible causes and the processes involved regarding the decrease in precipitation intensity or the total omission of convection with respect to the reference simulation in the absence of the Dead Sea water. Two main components, strongly affected by the drying out of the Dead Sea, are found to be highly relevant for the understanding of the environmental processes in the Dead Sea region.

(a) First, the lower-atmospheric boundary layer conditions. Changes in the energy balance affect the atmosphere through the heat exchange and moisture supply. The drying of the Dead Sea in the SEN simulations and the resulting decrease in local evaporation, impact the Dead Sea Basin conditions and the neighbouring areas. A reduction in boundary layer humidity and an increase in temperature result in a general decrease of atmospheric instability and weaker updrafts indicating reduced deep-convective activity. Main differences on the atmospheric conditions are directly over the Dead Sea, but these conditions are frequently advected to neighbouring areas by the

588 thermally driven wind systems in the region which play a key role for the redistribution
589 of these conditions and the initiation of convection.

590 (b) Secondly, wind systems in the valley. In the arid region of the Dead Sea Basin with
591 varied topography, thermally and dynamically driven wind systems are key features of
592 the local climate. Three different scales of climatic phenomena coexist: The
593 Mediterranean Sea Breeze (MSB), the Dead Sea breeze and the orographic winds,
594 valley-, and slope-winds, which are known to temper the climate in the Dead Sea valley
595 (Shafir and Alpert, 2011). The drying of the Dead Sea in the SEN simulation disturbs
596 the Dead Sea thermally driven wind circulations. The Dead Sea breezes are missing,
597 weaker wind speeds characterize the region and along valley winds are consequently
598 affected. Furthermore, the dynamics of the Mediterranean breeze penetration into the
599 Jordan Valley are affected.

600

601 Consequently, the impacts on convection initiation and development are twofold:
602 (i) Distinct redistribution of atmospheric conditions, locally or remotely, which yields to
603 different atmospheric conditions that in the absence of the Dead Sea result in a
604 reduced moisture availability in the lower atmospheric levels and increased stability
605 hindering convection or reducing the intensity of the events.
606 (ii) Modification of the divergence/convergence field. The absence of the Dead Sea
607 substantially modifies the wind circulation systems over the Dead Sea valley, which
608 leads to the omission of convergence lines which act as triggering mechanism for
609 convection.

610

611 We can conclude that in general the lack of sufficient low-atmospheric moisture in
612 relation to the drying out of the Dead Sea, the increase of atmospheric stability in
613 addition to an absence or reduction in the intensity of the convergence zones, works
614 against initiation or intensification of precipitating convection in the area. The relevance
615 of the small-scale variability of moisture and the correct definition and location of
616 convergence lines for an accurate representation of convective initiation illustrates the
617 limitation and the lack of adequate observational networks in the area and the need for
618 high-resolution model simulations of boundary layer processes to predict intense and
619 localised convection in the region.

620 These results contribute to gain a better understanding of the sensitivity of local
621 conditions in the Dead Sea valley and neighbouring areas to lake level decline. Energy
622 balance partitioning and wind circulation systems are determinant for local climatic
623 conditions, e.g. temperature and humidity fields as well as aerosol redistribution,

624 therefore, any change should be well understood and properly represented in model
625 simulations of the region. Our results point out, in agreement with past modelling
626 activities in the region, the need to further improve the representation of precipitation
627 fields in the area, particularly close to the Mediterranean coastline. More accurate
628 Mediterranean SST input fields have been suggested as relevant to reduce the model
629 inaccuracies. Furthermore, a more realistic representation of the lake shape, water
630 salinity and temperature, as well as Dead Sea abundance and depth must be
631 addressed to more accurately describe present and expected future conditions. In the
632 present study, limitations found in this direction in relation to model and external data
633 set descriptions, as well as identified biases regarding for example moisture sources
634 for HP in the region, MSB and Dead Sea evaporation, are expected to impact our
635 results, and have to be improved in future efforts in the region. In a further step, the
636 authors will investigate some of these issues in more detail, and will assess the impact
637 of model grid resolution on the horizontal and vertical flow field in the region across
638 scales, including the impact on large-scale dynamics. We will also put emphasis in
639 trying to better understand the dynamics of the MSB under lake level decline using
640 high-resolution modelling, especially the contrasting behaviour pointed out in this study.
641 Fine resolution simulations up to 100 m will be performed for this purpose.
642 Furthermore, we will provide a verification of the complex chain of processes in the
643 area using unique measurements in the framework of the interdisciplinary virtual
644 institute Dead Sea Research VEnue (DESERVE; Kottmeier et al., 2016).

645

Author contribution

647 SK wrote the manuscript, analysed the data, interpreted the results and supervised the
648 work. JH carried out data analysis, interpretation of results and prepared all the figures.

649

Acknowledgements

651 The first author's research was supported by the Bundesministerium für Bildung und
652 Forschung (BMBF; German Federal Ministry of Education and Research). The authors
653 acknowledge the colleagues at the Karlsruhe Institute of Technology (KIT) involved in
654 the interdisciplinary virtual institute Dead Sea Research VEnue (DESERVE) for their
655 support and interesting discussions. We acknowledge Sebastian Helgert and Alberto
656 Caldas Alvarez for their assistance in the preparation of the simulations. This article is
657 a contribution to the HyMeX program.

658

659   **References**

660   Alpert, P., and Shay-EL, Y.,: The Moisture Source for the Winter Cyclones in the
661   Eastern Mediterranean. Israel Meteorological Research Papers, 5, 20-27, 1994.

662   Alpert, P., and Coauthors: Relations between climate variability in the Mediterranean
663   region and the tropics: ENSO, South Asian and African monsoons, hurricanes
664   and Saharan dust. Developments in Earth and Environmental Sciences, 4, 149-
665   177, https://doi.org/10.1016/S1571-9197(06)80005-4, 2006.

666   Alpert, P., Shafir, H., and Issahary, D.,: Recent Changes in the Climate At the Dead
667   Sea – a Preliminary Study. Climatic Change, 37(3), 513-537,
668   https://doi.org/10.1023/A:1005330908974, 1997.

669   Andersson, T., Andersson, M., Jacobsson, C., Nilsson, S.: Thermodynamic
670   indices for forecasting thunderstorms in southern Sweden. Meteorol. Mag.
671   116, 141-146, 1989.

672   Arkin, Y., and Gilat, A.: Dead Sea sinkholes - an ever-developing hazard.
673   Environmental Geology, 39(7), 711-722,
674   https://doi.org/10.1007/s002540050485, 2000.

675   Ashbel, D., and Brooks, C.: The influence of the dead sea on the climate of its
676   neighbourhood. Quarterly Journal of the Royal Meteorological Society, 65(280),
677   185-194, https://doi.org/10.1002/qj.49706528005, 1939.

678   Ban, N., Schmidli, J., and Schär, C.: Evaluation of the convection-resolving
679   regional climate modeling approach in decade-long simulations, J. Geophys.
680   Res. Atmos., 119, 7889– 7907, https://doi.org/10.1002/2014JD021478, 2014.

681   Belachsen, I., Marra, F., Peleg, N., and Morin, E.: Convective rainfall in dry climate:
682   relations with synoptic systems and flash-flood generation in the Dead Sea
683   region. Hydrology and Earth System Sciences Discussions, 21, 5165-5180,
684   https://doi.org/10.5194/hess-21-5165-2017, 2017.

685   Böhm, U., and Coauthors: The Climate Version of LM: Brief Description and Long-
686   Term Applications. COSMO Newsletter, 6, 225-235, 2006.

687   Businger, J., Wyngaard, J., Izumi, Y., and Bradley, E.: Flux-Profile Relationships in the
688   Atmospheric Surface Layer. Journal of the Atmospheric Sciences, 28(2), 181-

189, https://doi.org/10.1175/1520-0469(1971)028<0181:FPRITA>2.0.CO;2, 1971.

Byun, H., and Kim, D.: Comparing the Effective Drought Index and the Standardized Precipitation Index. Options Méditerranéennes. Séries A. Mediterranean Seminars, 95, 85-89, 2010.

Byun, H., and Wilhite, D.: Objective quantification of drought severity and duration. J. Climate, 12(9), 2747-2756, https://doi.org/10.1175/1520-0442(1999)012<2747:OQODSA>2.0.CO;2, 1999.

Cohen, S., and Stanhill, G.: Contemporary Climate Change in the Jordan Valley. J. Appl. Meteor., 35(7), 1051-1058, https://doi.org/10.1175/1520-0450(1996)035<1051:CCCITJ>2.0.CO;2, 1996.

Corsmeier, U., Behrendt, R., Drobinski, P., Kottmeier, C.: The mistral and its

effect on air pollution transport and vertical mixing, Atmos. Res., 74, 275–302,

https://doi.org/https://doi.org/10.1016/j.atmosres.2004.04.010, 2005.

Dayan, U., and Morin, E.: Flash flood – producing rainstorms over the Dead Sea: A review. Geological Society of America, 401(4), 53-62, https://doi.org/10.1130/2006.2401(04) , 2006.

Dayan, U., and Sharon, D.: Meteorological parameters for discriminating between widespread and spotty storms in the Negev. Israel Journal of Earth Sciences, 29(4), 253-256, 1980.

Dayan, U., Ziv, B., Margalit, A., Morin, E., and Sharon, D.: A severe autumn storm over the middle-east: synoptic and mesoscale convection analysis. Theoretical and Applied Climatology, 69(1-2), 103-122, https://doi.org/10.1007/s007040170038, 2001.

Doms, G., and Baldauf, M.: A Description of the Nonhydrostatic Regional COSMO-Model. Part I: Dynamics and Numerics. Deutscher Wetterdienst, 2015.

Doswell, C., and Rasmussen, E.: The Effect of Neglecting the Virtual Temperature Correction on CAPE Calculations. Weather and Forecasting, 9(4), 625-629, https://doi.org/10.1175/1520-0434(1994)009<0625:TEONTV>2.0.CO;2, 1994.

FAO/IIASA/ISRIC/ISSCAS/JRC.: Harmonized World Soil Database (version 1.2). FAO, Rome, Italy and IIASA, Laxenburg, Austria, (accessed 01.02.2017) , 2009.

Fosser, G., Khodayar, S., and Berg, P., 2014: Benefit of convection permitting climate

721   model simulations in the representation of convective precipitation, Clim. Dyn.,

722   44(1– 2), 45– 60.

723   Gavrieli, I., Bein, A., and Oren, A., 2005: The expected impact of the "Peace Conduit"

724   project (the Red Sea - Dead Sea pipeline) on the Dead Sea. Mitigation and

725   Adaptation Strategies for Global Change, 10(4), 759-777,

726   https://doi.org/10.1007/s11027-005-5144-z.

727   European Commission, Joint Research Centre, 2003: Global Land Cover 2000

728   database, (accessed 01.02.2017).

729   GLOBE National Geophysical Data Center, 1999: Global Land One-kilometer Base

730   Elevation (GLOBE) v.1. Hastings, D. and P.K. Dunbar. National Geophysical

731   Data Center, NOAA, (accessed 01.02.2017).

732   Greenbaum, N., Ben-Zvi, A., Haviv, I., and Enzel, Y., 2006: The hydrology and

733   paleohydrology of the Dead Sea tributaries. Geological Society of America,

734   401(4), 63-93, https://doi.org/10.1130/2006.2401(05).

735   Haylock, M.R., Hofstra, N., Klein Tank, A.M.G., Klok, E.J., Jones, P.D. and New, M.

736   2008, A European daily high-resolution gridded dataset of surface temperature and

737   precipitation. Journal of Geophysical Research: Atmospheres, 113, D20119.

738   https://doi.org/10.1029/2008JD10201.

739

740   Hochman, A., Mercogliano, P., Alpert, P., Saaroni, H. and Bucchignani, E., 2018. High-

741   resolution projection of climate change and extremity over Israel using COSMO-CLM.

742   International Journal of Climatology, 38(14), pp.5095-5106.

743

744   Houze, R., 2012: Orographic effects on precipitating clouds. Reviews of Geophysics,

745   50(1), https://doi.org/10.1029/2011RG000365.

746   Kalthoff, N., Horlacher, V., Corsmeier, U., Volz-Thomas, A., Kolahgar, B., Geiß, H.,

747   Möllmann-Coers, M., and Knaps, A. 2000: Influence of valley winds on transport

748   and dispersion of airborne pollutants in the Freiburg-Schauinsland area, J.

749   Geophys. Res. Atmos, 105, 1585–1597, https://doi.org/10.1029/1999jd900999.

750

751   Khodayar, S., Kalthoff, N., and Schaedler, G., 2013: The impact of soil moisture

752   variability on seasonal convective precipitation simulations. Part I: validation,

753   feedbacks, and realistic initialisation. Meteorologische Zeitschrift, 22(4), 489-505,

754   https://doi.org/10.1127/0941-2948/2013/0403.

Kunin, P., Alpert, P. and Rostkier-Edelstein, D., 2019. Investigation of sea-breeze/foehn in the Dead Sea valley employing high resolution WRF and observations. Atmospheric Research.

Lensky, N. and Dente, E., 2015. The hydrological proecesses driving the accelerated Dead Sea level decline in the past decades. Geological Survey of Israel Report.

Llasat, M., and Coauthors, 2010: High-impact floods and flash floods in Mediterranean countries: the FLASH preliminary database. Advances in Geosciences, 23, 47-55, https://doi.org/10.5194/adgeo-23-47-2010.

Metzger, J., Nied, M., Corsmeier, U., Kleffmann, J., and Kottmeier, C., 2017: Dead Sea evaporation by eddy covariance measurements versus aerodynamic, energy budget, Priestley-Taylor, and Penman estimates. Hydrology and Earth System Sciences Discussions, 22(2), 1135-1155, https://doi.org/10.5194/hess-2017-187.

Miglietta MM, Conte D, Mannarini G, Lacorata G, Rotunno R. 2011. Numerical analysis of a Mediterranean 'hurricane' over south-eastern Italy: sensitivity experiments to sea surface temperature. *Atmos. Res.* **101**: 412–426.

Moncrieff, M., and Miller, M., 1976: The dynamics and simulation of tropical cumulonimbus and squall lines. Quarterly Journal of the Royal Meteorological Society, 102(432), 373-394, https://doi.org/10.1002/qj.49710243208, 2014.

Naor, R., Potchter, O., Shafir, H., and Alpert, P.: An observational study of the summer Mediterranean Sea breeze front penetration into the complex topography of the Jordan Rift Valley, Theor. Appl. Climatol., 127, 275–284, https://doi.org/10.1007/s00704-015-1635-3, 2017.

Prein, A., Gobiet, A., Suklitsch, M., Truhetz, H., Awan, N., Keuler, K., and Georgievski, G. : Added value of convection permitting seasonal simulations, Clim. Dyn., 41(9– 10), 2655– 2677, 2013.

Ritter, B., and J.-F. Geleyn, 1992. A comprehensive radiation scheme for numerical weather prediction models with potential applications in climate simulations. Mon. Wea. Rev., 120, 303–325.

787 Rostkier-Edelstein, D., Liu, Y., Wu, W., Kunin, P., Givati, A. and Ge, M., 2014. Towards

788 a high-resolution climatography of seasonal precipitation over Israel. International

789 Journal of Climatology, 34(6), pp.1964-1979.

790

791 Schaedler, G., and Sasse, R.: Analysis of the connection between precipitation and

792 synoptic scale processes in the Eastern Mediterranean using self-organizing maps.

793 Meteorologische Zeitschrift, 15(3), 273-278, https://doi.org/10.1127/0941-

794 2948/2006/0105, 2006.

795 Shafir, H., and Alpert, P.: Regional and local climatic effects on the Dead-Sea

796 evaporation. Climatic Change, 105(3-4), 455-468,

797 https://doi.org/10.1007/s10584-010-9892-8, 2011.

798 Sharon, D., and Kutiel, H.: The distribution of rainfall intensity in Israel, its regional and

799 seasonal variations and its climatological evaluation. International Journal of

800 Climatology, 6(3), 277-291, https://doi.org/10.1002/joc.3370060304, 1986.

801 Smiatek, G., Kunstmann, H., and Heckl, A.: High-resolution climate change simulations

802 for the Jordan River area. Journal of Geophysical Research, 116(D16),

803 https://doi.org/10.1029/2010JD015313, 2011.

804 Stanhill, G.: Changes in the rate of evaporation from the dead sea. International

805 Journal of Climatology, 14(4), 465-471,

806 https://doi.org/10.1002/joc.3370140409,1994.

807 Vicente-Serrano, S., Beguería, S., López-Moreno, J.: A Multiscalar Drought Index

808 Sensitive to Global Warming: The Standardized Precipitation

809 Evapotranspiration Index. J. Climate, 23(7), 1696-1718,

810 https://doi.org/10.1175/2009JCLI2909.1, 2010.

811 Vüllers, J., Mayr, G. J., Corsmeier, U., and Kottmeier, C.: Characteristics and

812 evolution of diurnal foehn events in the Dead Sea valley. Atmos. Chem. Phys.,

813 18, 18169-18186, https://doi.org/10.5194/acp-18-18169-2018, 20, 2018.

814

815 Wernli H, Paulat M, Hagen M, Frei C. SAL – a novel quality measure for the

816 verification of quantitative precipitation forecasts. Mon. Weather Rev. 136: 4470–

817 4487, 2008.

818

819 Yatagai, A., Alpert, P. and Xie, P. (2008) Development of a daily gridded precipitation

820 data set for the Middle East. Advances in Geosciences, 12, 1–6.

821

822 Yatagai, A., Kamiguchi, K., Arakawa, O., Hamada, A., Yasutomi, N. and Kitoh, A.,

823 2012: APHRODITE: constructing a long-term daily gridded precipitation dataset for

824 Asia based on a dense network of rain gauges. Bulletin of the American Meteorological

825 Society, 93, 1401–1415.

826

827

828

829

830

831

832

833

834

835

836

837

838

839

840

841

842

843

844

845

Tables

	PREC diffmn	REF PMX	SEN PMX	PREC relative diff [%]	Synoptic Situation	REF CAPEmx	SEN CAPEmx	REF KOmn	SEN KOmn	Localised/ Widespread (Subarea affected)
08.12.2004	0,10	30,09	31,31	2,76	ARST	1	1	4,85	4,85	W (A1, A2)
13.01.2006	-0,11	45,64	54,64	-4,26	Cyprus Low	239	225	6,57	6,54	L/W (A1, A3)
16.04.2006	0,11	57,41	56,09	4,89	Syrian Low	43	47	1,97	1,94	L (A1, A4)
10.04.2007	0,29	42,61	70,20	30,78	Cyprus Low	686	679	-4,77	-4,70	L (A2, A4)
13.04.2007	0,12	134,36	127,79	1,62	Cyprus Low	573	576	-1,95	-1,92	L (A1, A2, A3, A4)
12.05.2007	-0,16	41,82	47,90	-8,24	Syrian Low	436	81	-5,30	-5,29	L (A1, A2)
27.01.2008	-0,14	23,11	17,24	-17,25	Syrian Low	7	7	5,12	5,12	W (A1, A3)
25.10.2008	-0,23	139,01	125,73	-16,52	ARST	1274	1361	-5,50	-4,08	L (A3)
13.11.2008	0,30	40,83	45,55	25,68	ARST	25	7	1,37	1,38	L (A2, A4)
14.05.2009	-0,39	59,28	68,84	-8,49	Syrian Low	433	429	-3,90	-3,91	L (A1, A2, A3, A4)
15.05.2009	0,20	49,23	42,28	13,50	Syrian Low	208	203	-2,30	-2,36	L (A1, A2, A3)
31.10.2009	-0,19	166,21	111,79	-7,65	Cyprus Low	435	445	-5,03	-4,46	L (A1, A2)
15.01.2011	0,11	73,02	72,03	3,74	Syrian Low	49	37	7,82	7,83	L/W (A1, A4)
28.05.2011	-0,24	44,51	32,73	-14,33	Cyprus Low	158	170	-10,27	-10,26	W (A2)
14.11.2011	-0,11	42,65	9,34	-65,90	Cyprus Low	2	0	-7,14	-7,12	L (A1, A2)
17.11.2011	0,11	90,07	93,04	4,76	Cyprus Low	386	304	-9,14	-9,16	L (A1)
18.11.2011	-0,11	28,68	34,69	-8,67	Cyprus Low	356	378	-8,61	-8,65	L (A1)
19.11.2011	0,03	58,11	12,36	4,09	Cyprus Low	133	81	-7,60	-7,46	L (A2, A4)
22.10.2012	0,20	29,88	41,64	51,21	ARST	2068	2097	-5,83	-5,59	L (A1, A2)
09.11.2012	-0,11	27,20	22,56	-18,29	Cyprus Low	218	215	3,97	3,98	W (A1)
23.11.2012	-0,21	155,77	117,81	-10,17	ARST	189	286	-2,18	-1,95	L (A1, A2, A3)
25.11.2012	-0,11	41,48	54,33	-7,87	ARST	354	332	4,19	4,37	L (A3, A4)

847

848

Table 1: Classification of heavy precipitation cases in the decadal simulation covering the period 2004 to 2013. The areal-mean (study area, Figure 1) difference (PREC$_{diffmn}$) and maximum grid precipitation in the reference (REF$_{PMX}$) and sensitivity (SEN$_{PMX}$) realizations, the precipitation relative difference in %, the synoptic situation, and the stability conditions illustrated by maximum grid point CAPE (CAPEmx) and minimum grid point KO-index (KOmn) are summarized. Additionally, the nature of the precipitation, localized (L) or widespread (W) and the main subarea affected (following division in Figure 1; A1, A2, A3, A4) are listed.

857

858

859

860

861

862

863

864

865

Figures

867   (a)

868

869   (b)

870

871
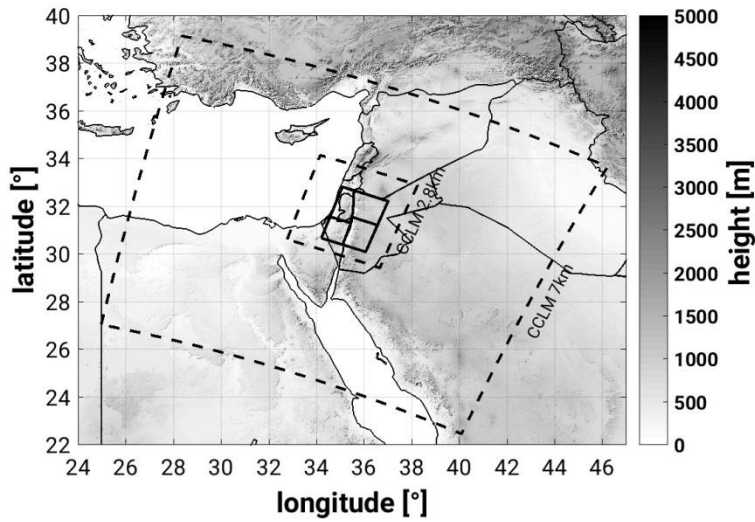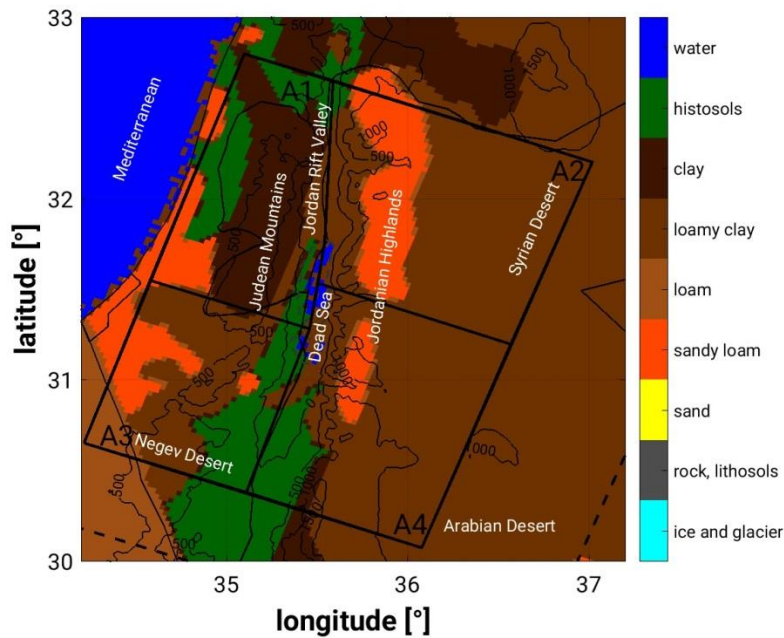
Figure 1: (a) Topography (m above msl), simulation domains (dashed lines, CCLM7km and CCLM2.8km) and study area (bold line). (b) Model soil types (colour scale), topography (black isolines) and study area (black bold line) including the 4 subdomains to be examined, A1-4 (Area 1-4).

876   (a)

877
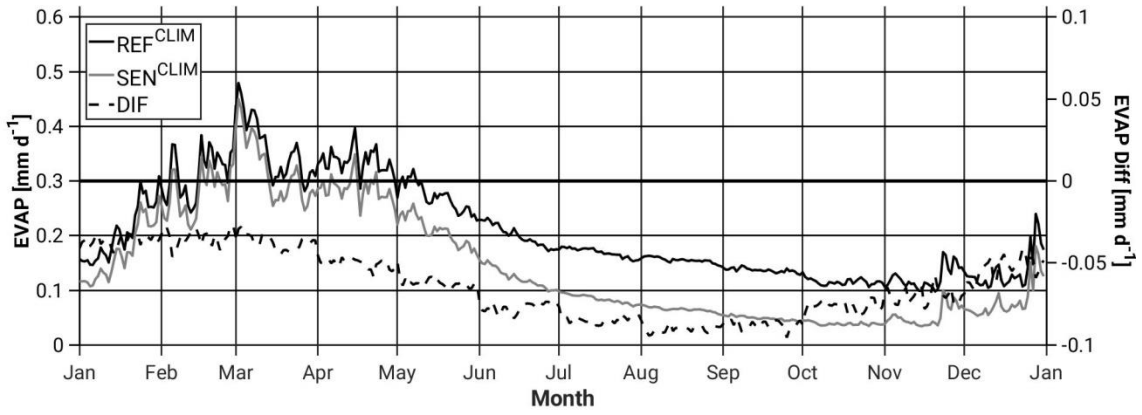
878
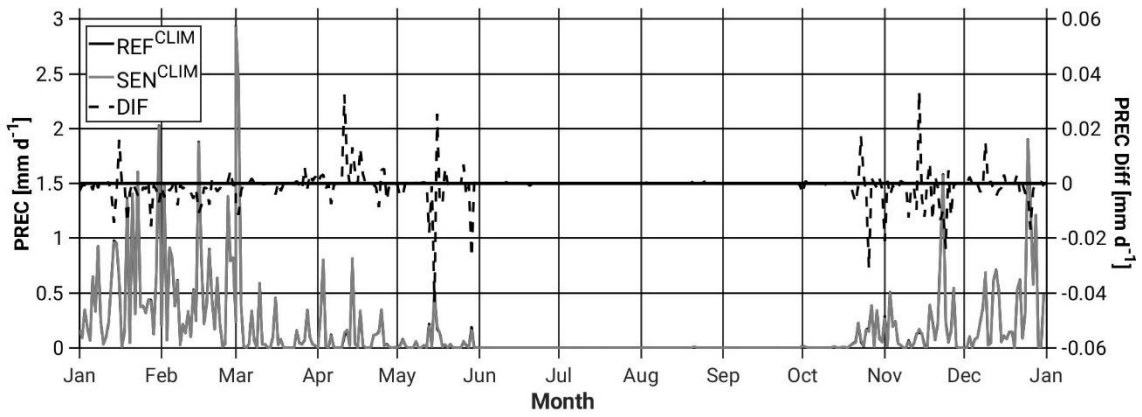
879

880
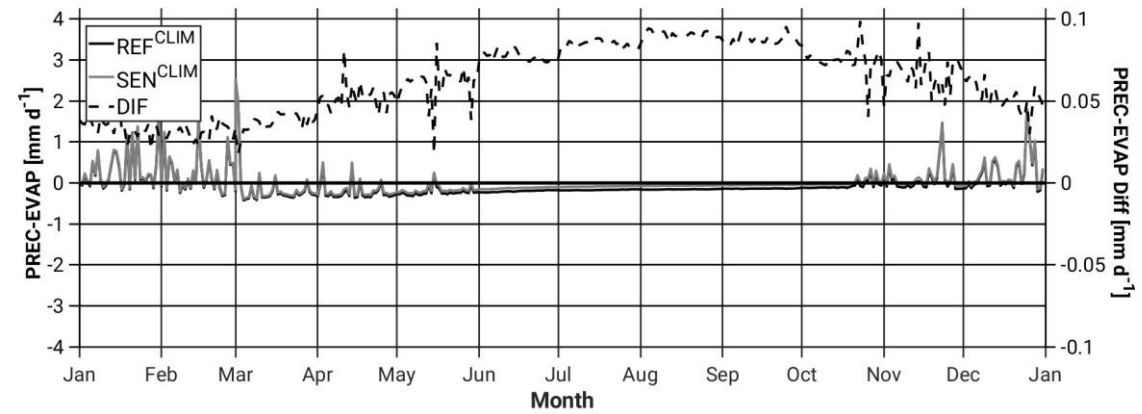
881

882

883

884

885

886

887

888

889   (b)
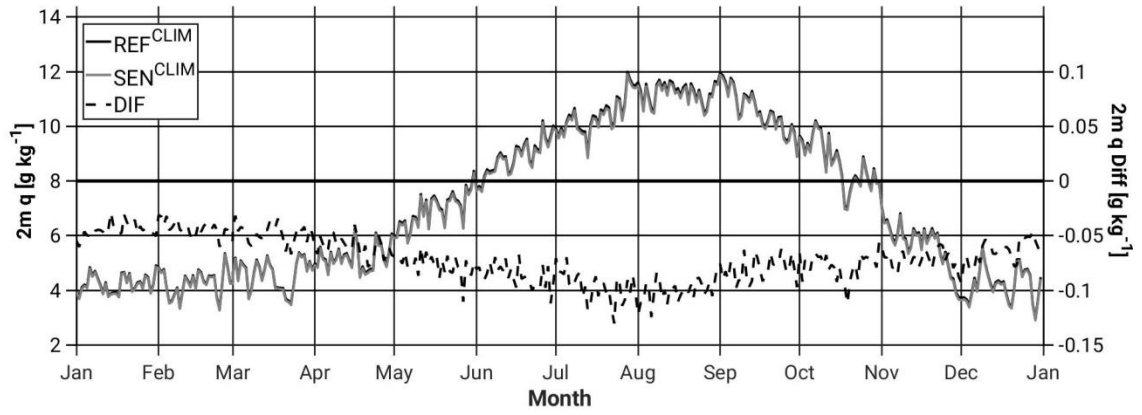
890

891
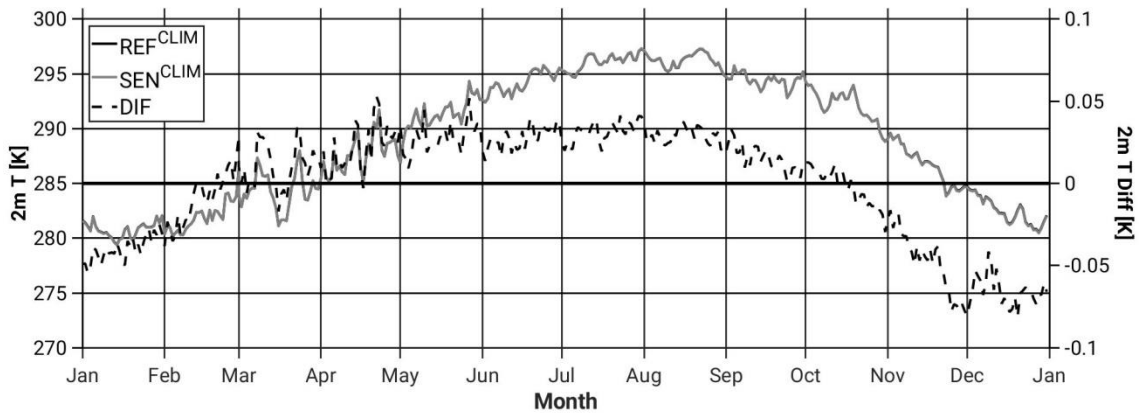
892

893

894

895

896

897

898

899

900

901

902

903

904

905   (c)

906
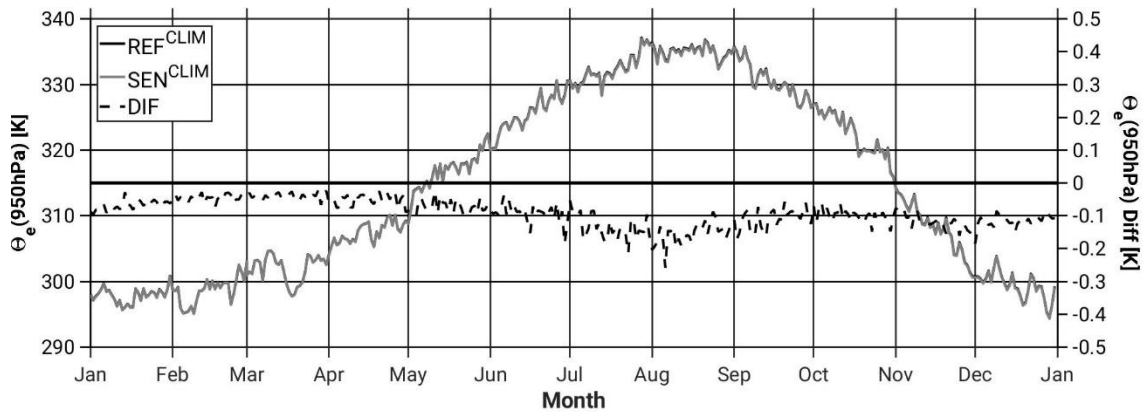
907
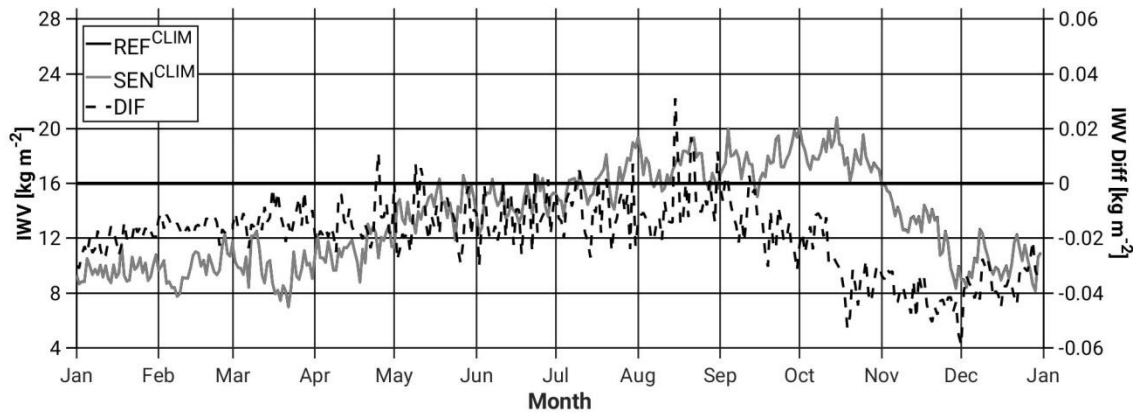
908

909

910

911

912

913

914

915

916

917

918

919

920

921

922

923   (d)

924
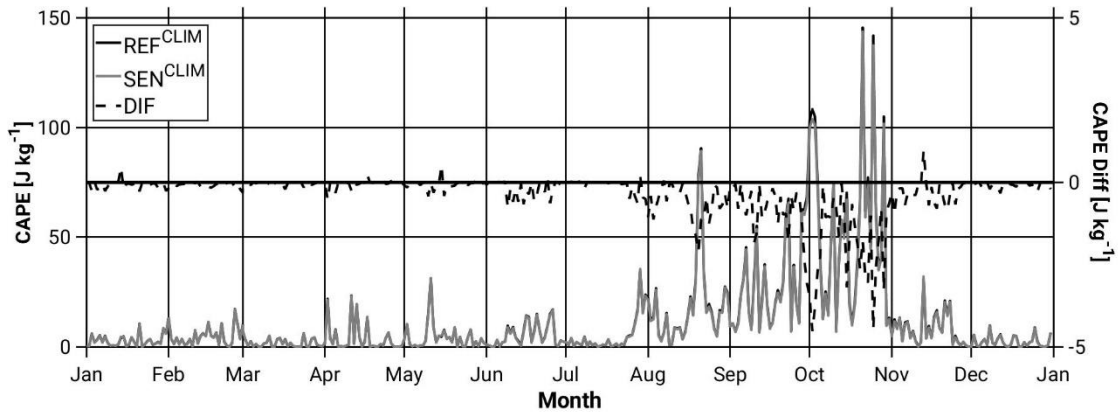
925
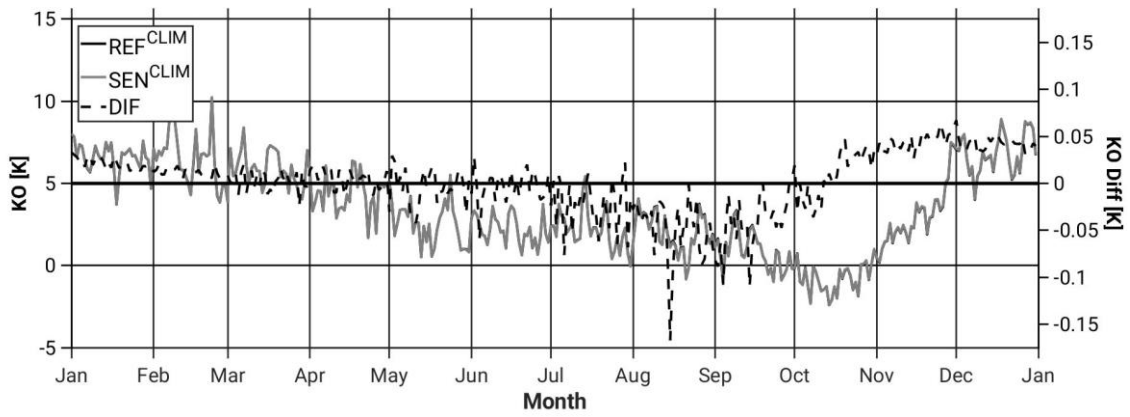
926

927

928

929   Figure 2: Annual cycle of the areal-daily averaged (and differences (black dashed line;
930   SEN-REF)) of (a) evaporation, precipitation, and precipitation minus evaporation (b)
931   specific humidity and temperature at 2-m, and (c) Θ_e below 950 hPa and IWV, and (d)
932   CAPE and KO-index, from the REF[CLIM] (full black line) and the SEN[CLIM] (full grey line)
933   simulations. All grid points in the study area (Figure 1) and the period 2004 to 2013 are
934   considered.

935

936

937

938

939

940

941   (a)
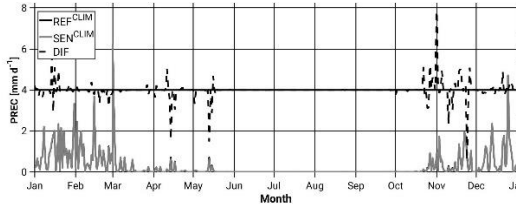
942   Area1 (NW)   Area2 (NE)
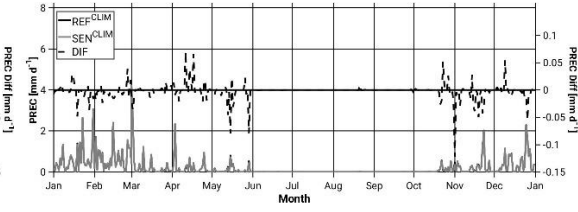
943
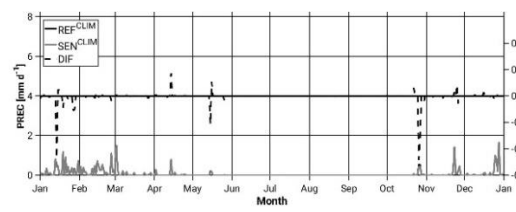
944   Area3 (SW)   Area4 (SE)
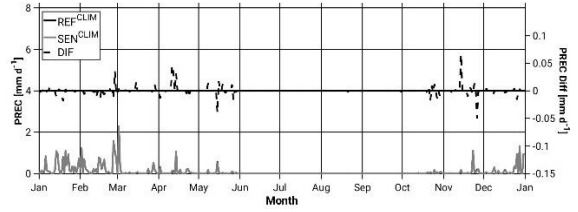
945

946   (b)
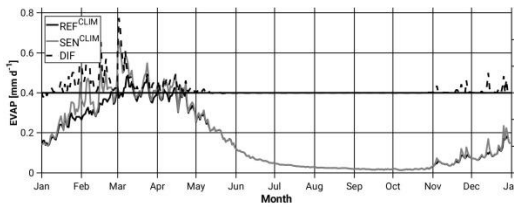
947   Area1 (NW)   Area2 (NE)
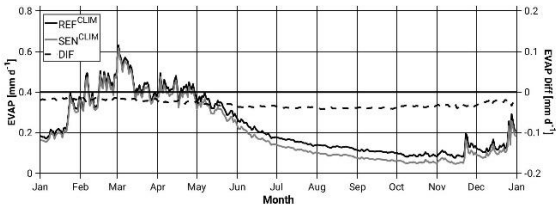
948
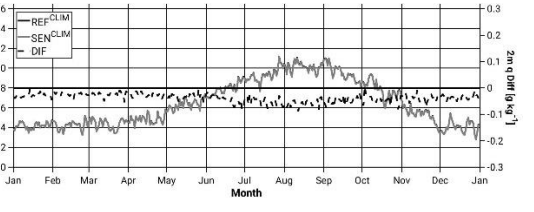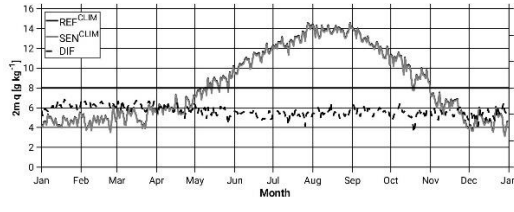
949
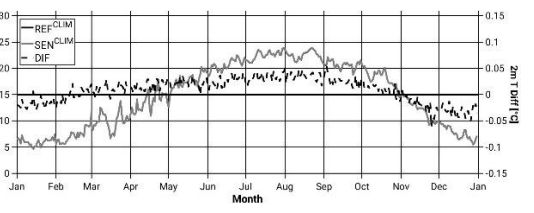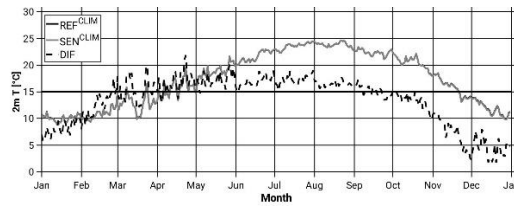
950
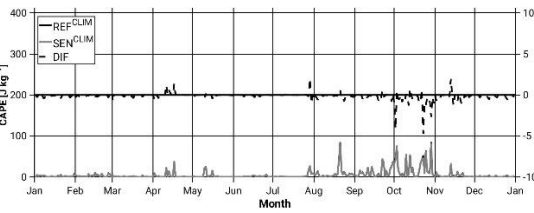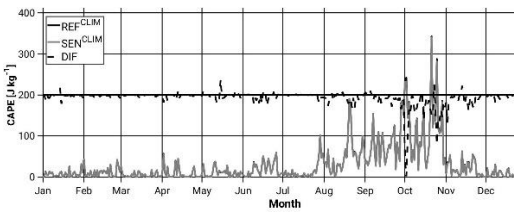
951

952

953

954 Figure 3: Annual cycle of the areal-daily averaged (and differences (black dashed line;
955 SEN-REF)) of (a) precipitation for areas A1, A2, A3, A4 (see Figure 1b), and (b)
956 evaporation, specific humidity and temperature at 2-m, and CAPE for areas A1 and A2,
957 from the REF^{CLIM} (full black line) and the SEN^{CLIM} (full grey line) simulations. Only land
958 points in the study area (Figure 1) for evaporation, and all grid points for the rest of
959 variables and the period 2004 to 2013 are considered.

960

961

962

963

964

965

966

967

968

969

970

971

972

973

974

975

976

977

978

979

980

981

982

983

984

985   (a)
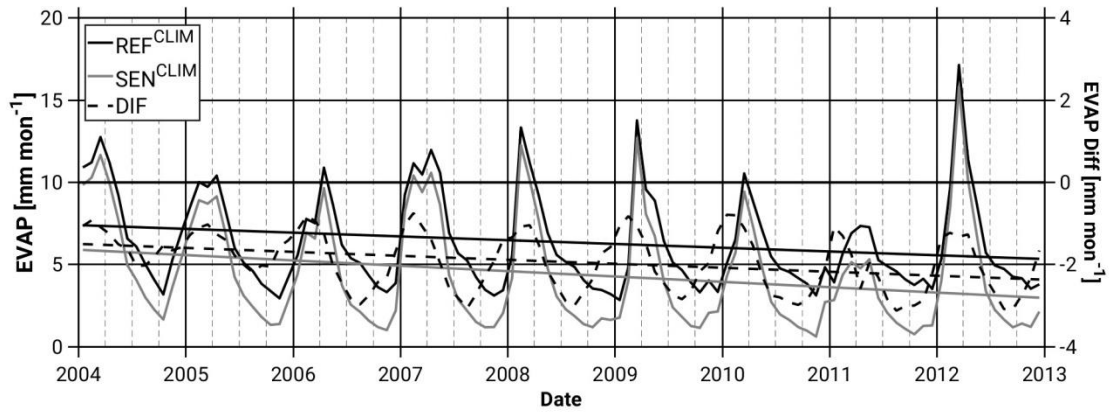
986

987   (b)
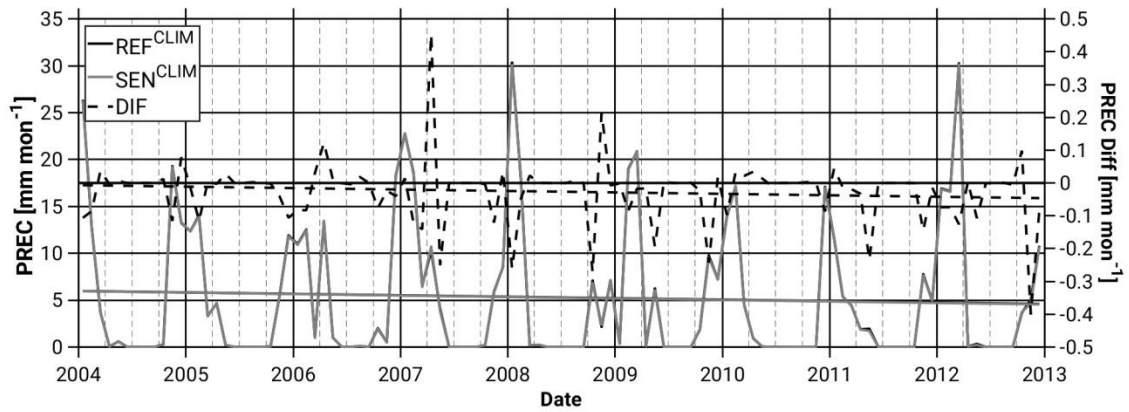
988

989   (c)
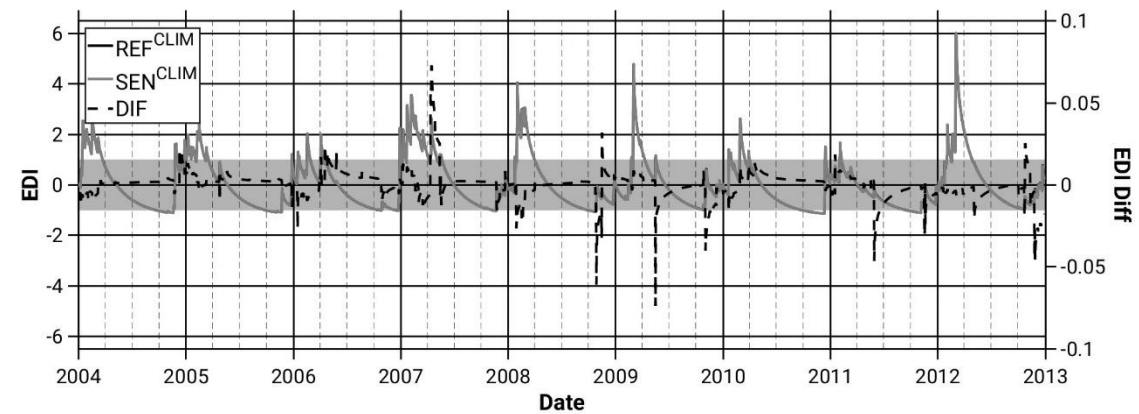
990

991   Figure 4: Temporal evolution of the monthly-daily accumulated areal mean values of
992   (a) Evaporation, (b) Precipitation, (c) Effective Drought Index (EDI), from the REF[CLIM]
993   (full black line) and the SEN[CLIM] (full grey line) simulations and differences depicted with
994   black dashed lines. The light grey band in (c) indicates the common soil state (-
995   1<EDI<+1). All grid points in the study area (Figure 1) and the period 2004 to 2013 are
996   considered.

997

998

999   (a)
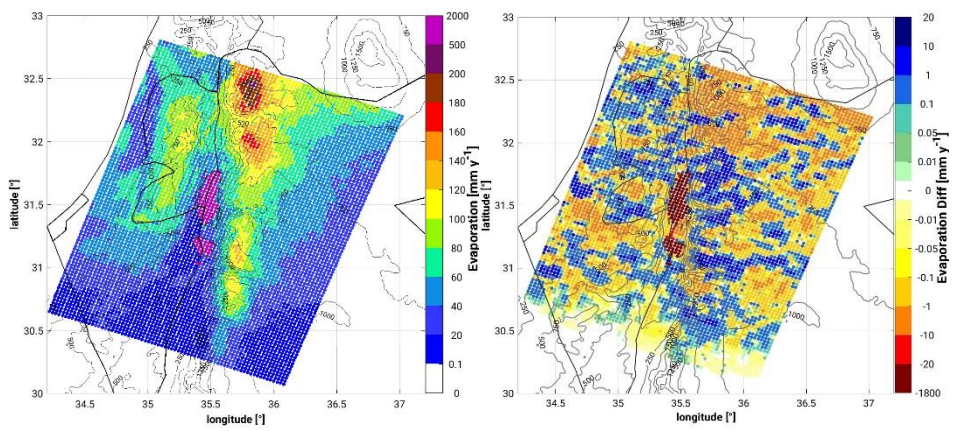
1000

1001

1002

1003   (b)
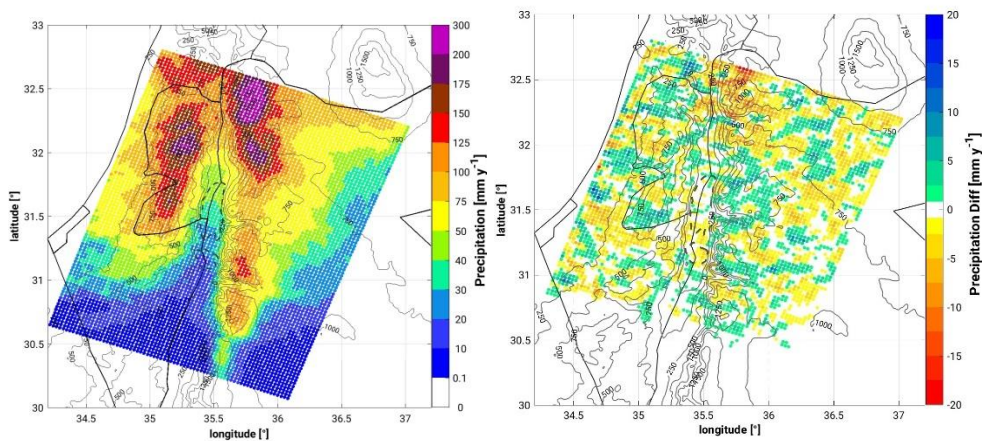
1004

1005

1006

1007   Figure 5: Spatial distribution of (a) evaporation in the REF[CLIM] simulation (left) and the
1008   difference between the SEN[CLIM] and the REF[CLIM] simulations (right), and (b)
1009   precipitation in the REF[CLIM] simulation (left) and the difference between the SEN[CLIM]
1010   and the REF[CLIM] simulations (right). The period 2004 to 2013 is considered.

1011

1012

1013

1014

1015 (a)   (b)
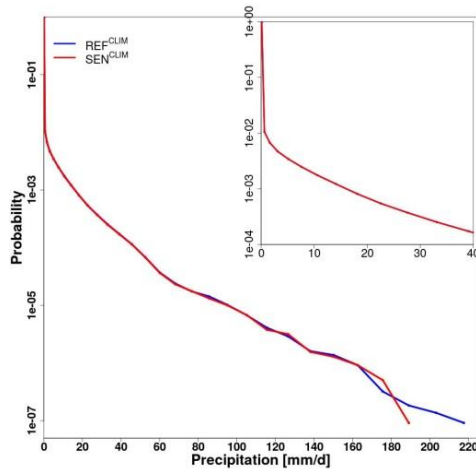
1016

1017

1018
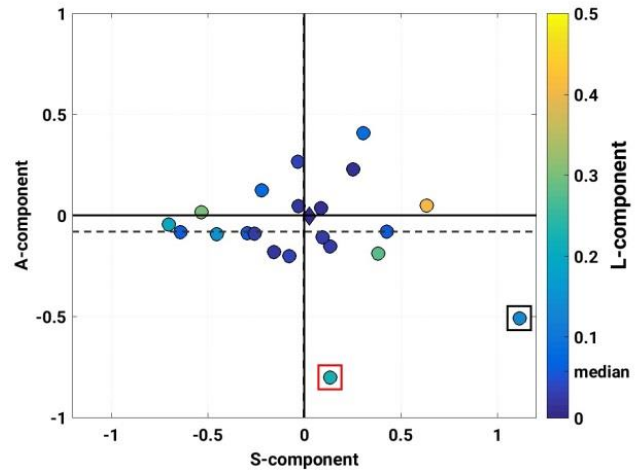
1019 Figure 6: (a) Probability density function of daily precipitation intensities. All grid points
1020 in the investigation domain (Figure 1) and the period 2004 to 2013 are considered. (b)
1021 SAL diagram between REF^{CLIM} and SEN^{CLIM} simulations. Every circle corresponds to a
1022 simulated heavy precipitation event (listed in Table 1). The diamond (close to the zero-
1023 zero) illustrates the mean of all events. A-component (amplitude), S-component
1024 (structure), L-component (location). The inner colour indicates the L-component. Boxes
1025 point out the two events examined in this study, CASE1 and CASE2 (see section 3.2).

1026

1027

1028

1029

1030

1031

1032

1033

1034

1035

1036

1037

1038

1039   (a)
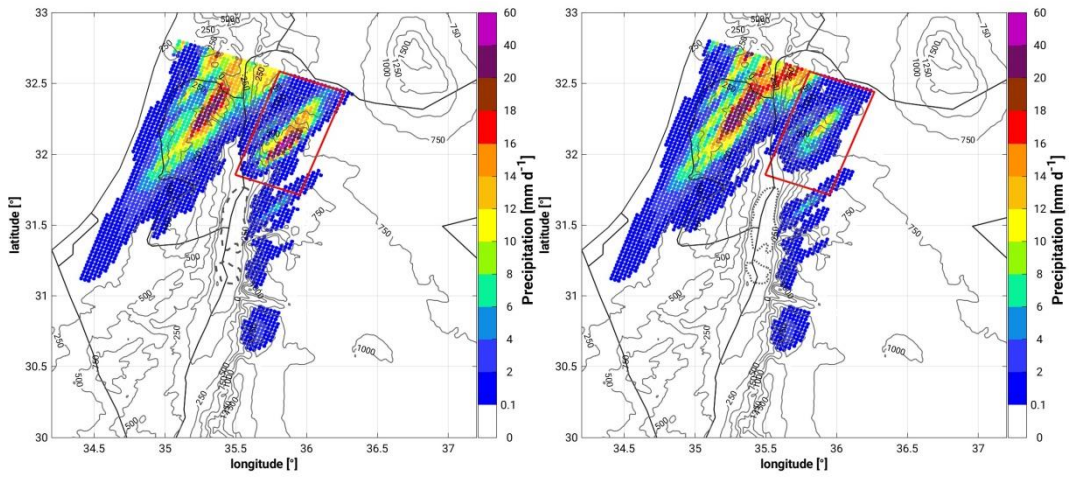
1040

1041   (b)
1042
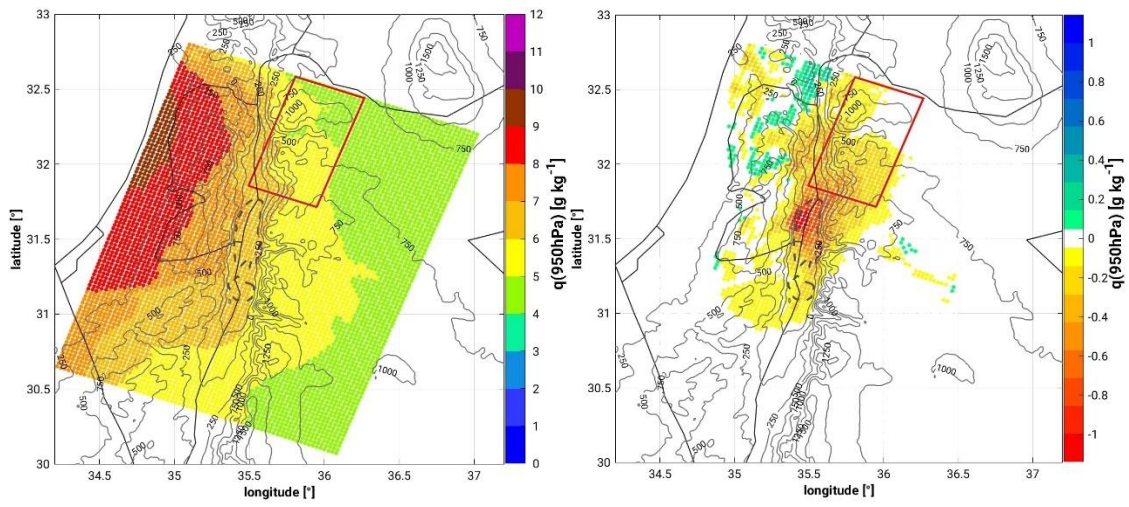
1043
1044

1045

1046

1047

1048

1049

1050

1051

1052   (c)
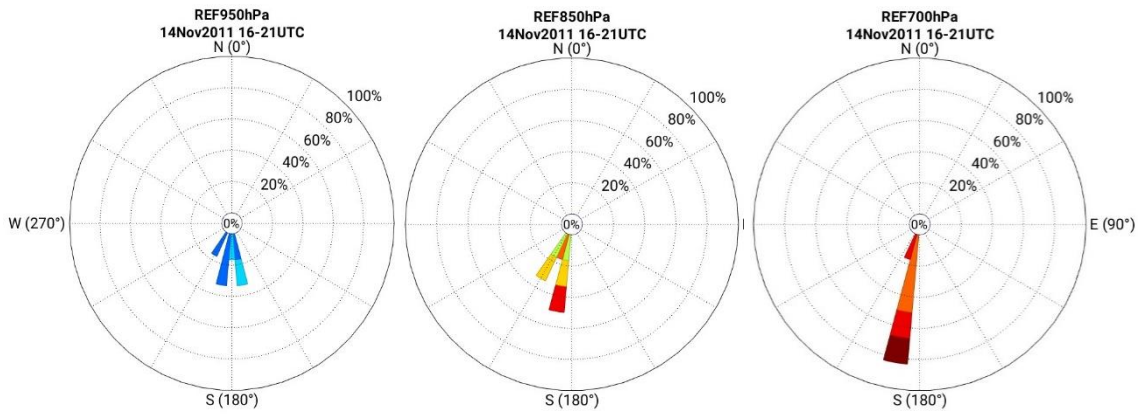
1053

1054
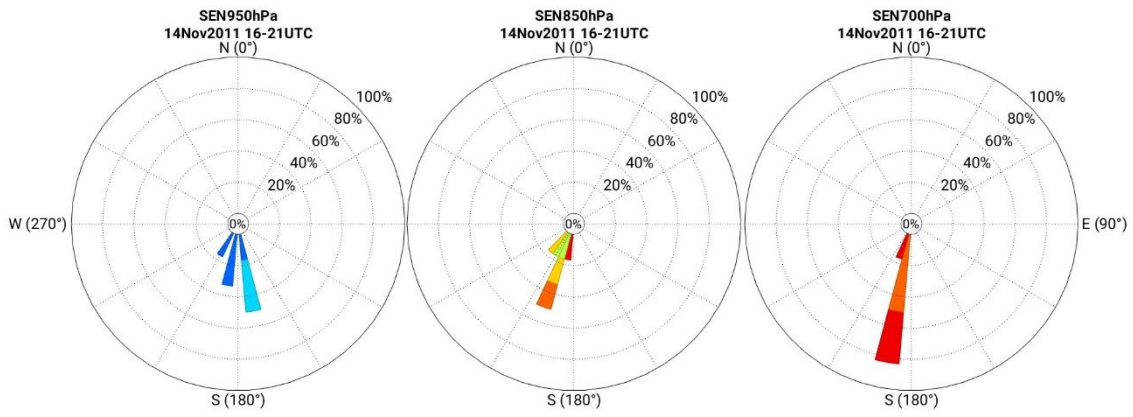
1055

1056

1057

1058

1059

1060

Figure 7: Spatial distribution of (a) 24-h accumulated precipitation from 14.11 09 UTC to 15.11 08 UTC from the REF[14.11] simulation (left) and the SEN[14.11] simulation (right) and (b) specific humidity below 950 hPa, from the REF[14.11] simulation (left) and the difference between the REF[14.11] and SEN[14.11] simulations, as a mean for the 6-h period prior to convection initiation in the target area (14 November 16 UTC to 21 UTC), and (c) wind conditions at 700 hPa, 850 hPa, and 950 hPa (no relevant differences with respect to the 10-m field) for the same time period. Wind roses are centred at about 35.82°E-32.07°N in our target area.

1092

1093   (a)
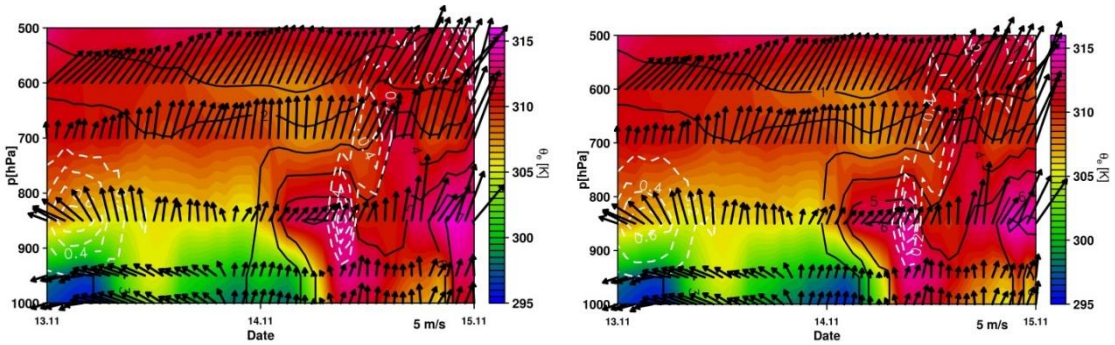
1094

1095   (b)

1096
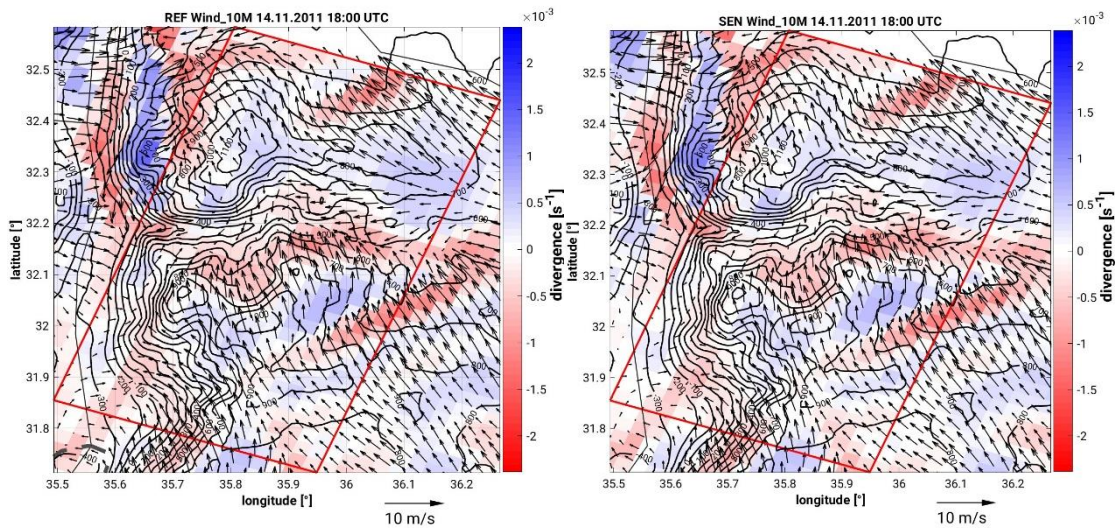
1097

1098

1099   Figure 8: (a) Vertical-temporal cross-section of equivalent potential temperature (colour
1100   scale; K), specific humidity (black isolines; g/kg), horizontal wind vectors (north-pointing
1101   upwards, m/s) and vertical velocity (white dashed contours with 0.1 m/s increments) of
1102   the REF[14.11] (left) and SEN[14.11] (right) simulations, over a representative grid point in the
1103   sub-study region, 32.05°N 35.79°E. (b) Spatial distribution of 10-m horizontal wind
1104   (wind vectors; m/s) and corresponding divergence/convergence field (colour scale; s[-1])
1105   at 18 UTC on the 14 November 2011 from the REF[14.11] (left) and SEN[14.11] (right)
1106   simulations.

1107

1108
1109
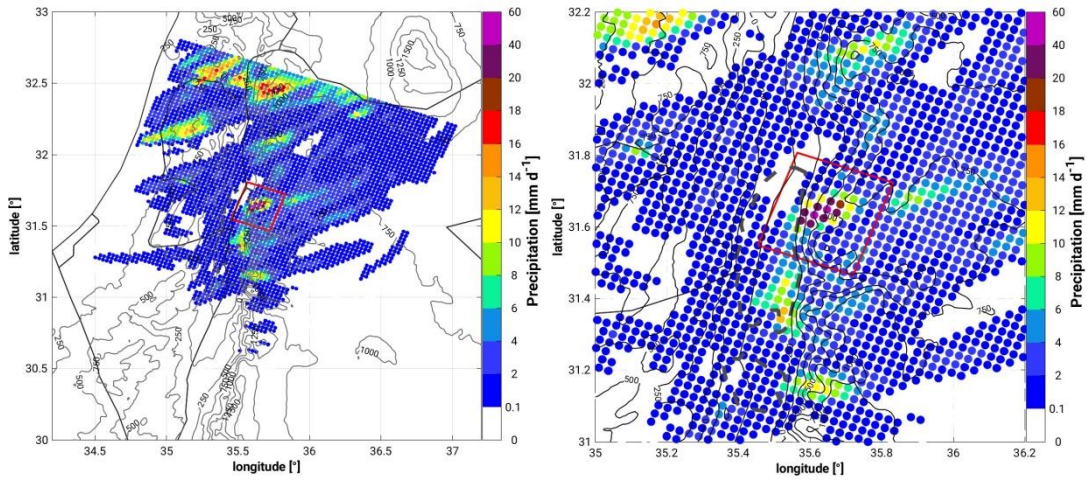
1110
1111
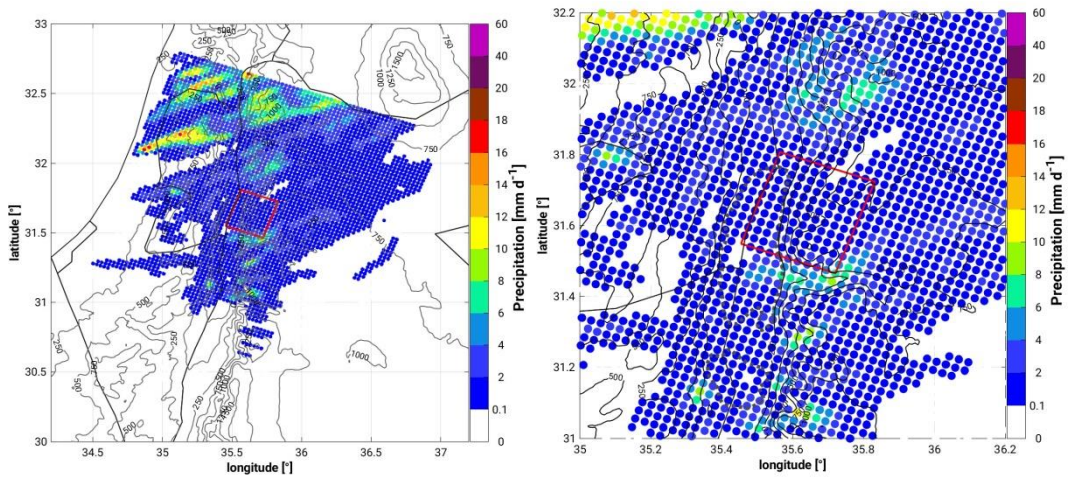
1112
1113
1114
1115

Figure 9: 24-h mean spatial distribution of precipitation from the REF[19.11] simulation
(top-left; zoom top-right) and the SEN[19.11] simulation (bottom-left; zoom bottom-right)
for the period 18 November 2011 11 UTC to 19 November 2011 10 UTC.

1116
1117
1118

1119

1120

1121

1122

1123

1124

1125

1126

1127   (a)
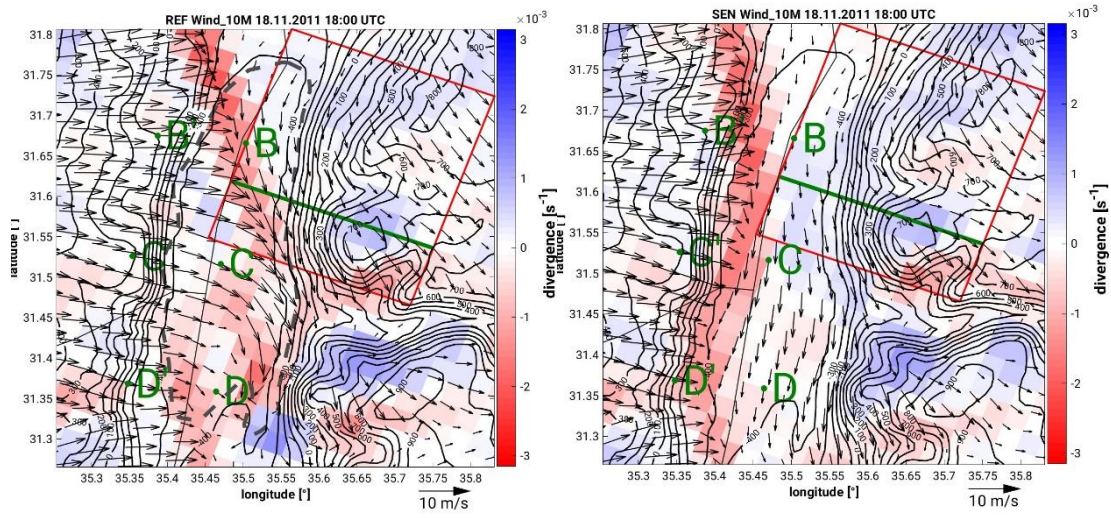
1128

1129   (b)
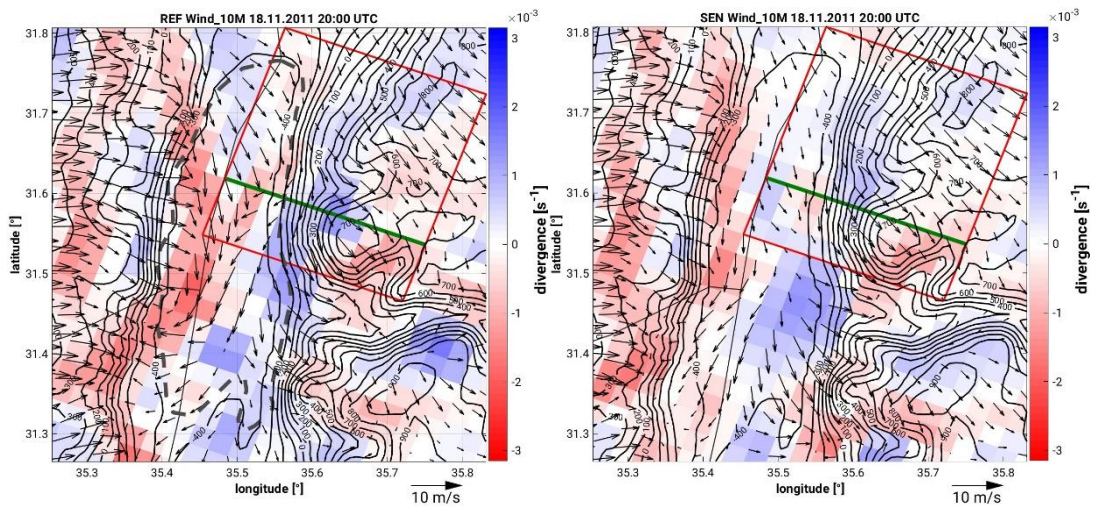
1130

1131

1132

1133

1134

1135

1136

1137

1138

1139   (c)
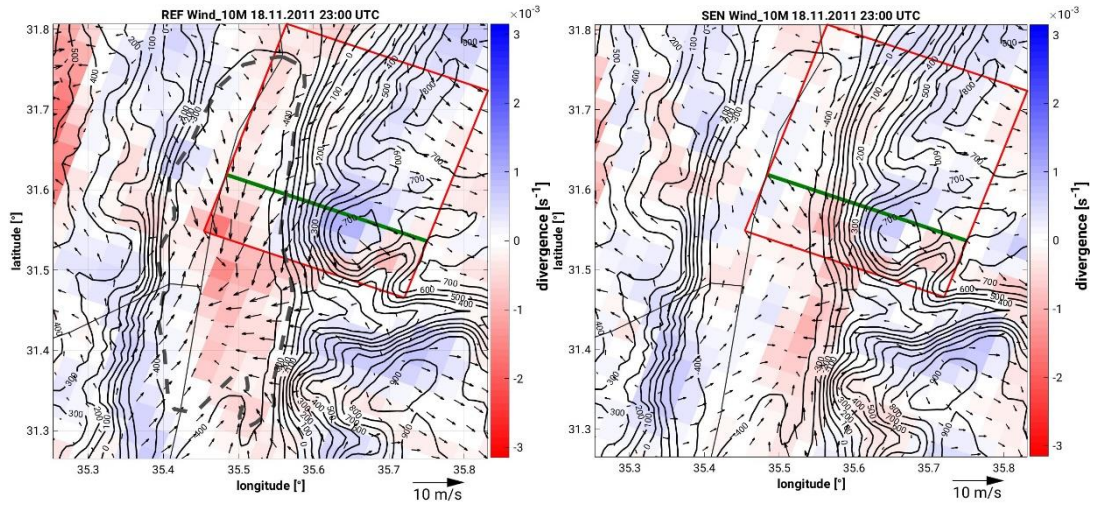
1140

1141

1142   (d)
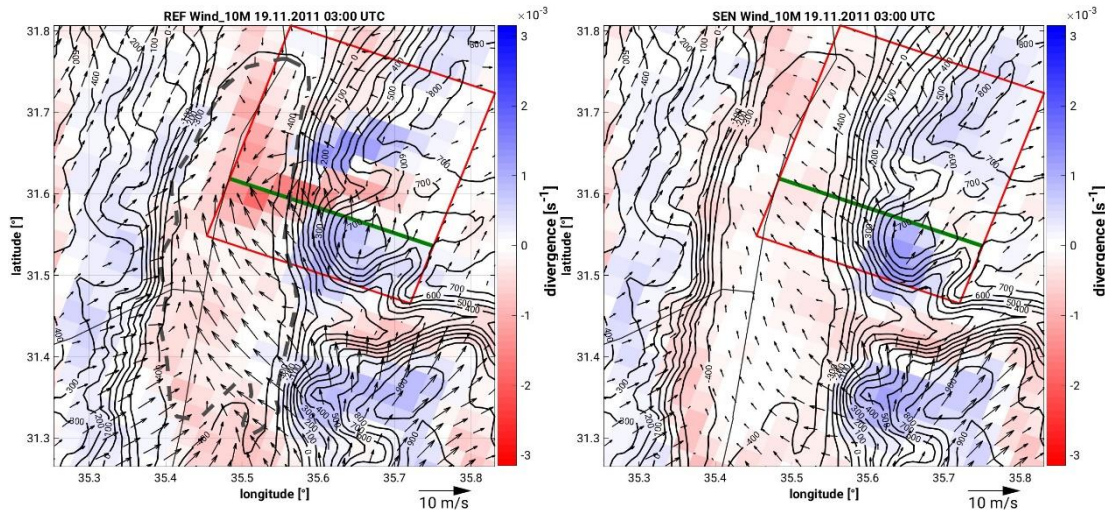
1143

1144

1145   Figure 10: Spatial distribution of 10-m horizontal wind (wind vectors; m/s) and
1146   corresponding divergence/convergence field (colour scale; s^{-1}) at 18 UTC, 20 UTC, 23
1147   UTC on the 19 November, and 03 UTC on the 20 November 2011 from the REF[19.11]
1148   (left) and SEN[19.11] (right) simulations. The topography is indicated by the black full
1149   isolines. The transects (B-C-D and B'-C'-D') corresponding to the locations in which
1150   temperature comparisons are made are indicated in Figure 10a. The green line
1151   indicates the position of the vertical cross-section in Figure 11.

1152

1153

1154
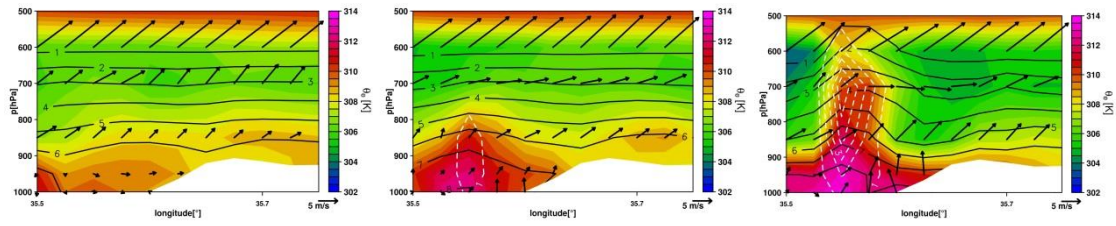
1155

1156
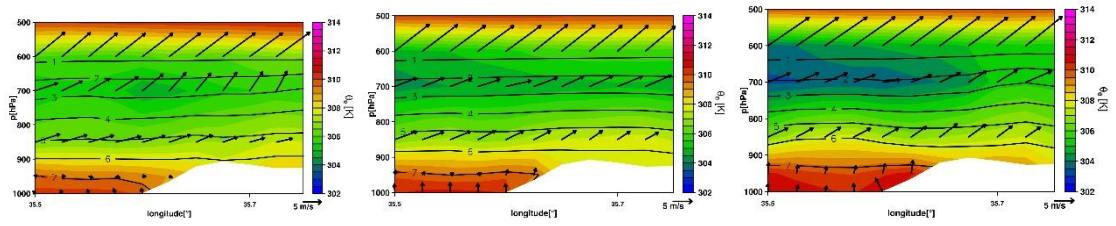
1157

1158

1159

Figure 11: Vertical cross-section of equivalent potential temperature (colour scale; K), specific humidity (black isolines; g/kg), horizontal wind vectors (north-pointing upwards, m/s) and vertical velocity (white dashed contours with 1 m/s increments) of the REF[19.11] (top) and SEN[19.11] (bottom) simulations at 01 UTC (left), 02 UTC (middle) and 03 UTC (right). The location of the cross-section is indicated in Figure 10.

1165

1166

1167

1168

1169

1170

1171

1172

1173

1174

1175